Science

AAAS

Supplementary Materials for

Chip-less wireless electronic skins by remote epitaxial freestanding compound semiconductors

Yeongin Kim *et al*.

Corresponding authors: Jiyeon Han, sviviria@amorepacific.com; Jeehwan Kim, jeehwan@mit.edu

The PDF file includes:

Materials and Methods
Supplementary Text
Figs. S1 to S24
Tables S1 and S2
References

Other Supplementary Material for this manuscript includes the following:

Movie S1

Materials and Methods

Production of GaN nanomembranes via remote homoepitaxy

  A Veeco Gen200 plasma-assisted molecular beam epitaxy system was used to grow GaN thin films on 2D materials coated GaN substrates. The GaN substrates are commercial 5 μm GaN grown on sapphire. Prior to growth, GaN substrates were cleaned with acetone, isopropanol (IPA), and hydrochloric acid (HCl) before loading into the reaction chamber. 1 ~ 3 layers of 2D materials were deposited on GaN substrates after being outgassed at 700 °C for 15 min. Then, 200 nm to 1.8 μm GaN epilayers were grown at substrate temperature from 680 °C to 730 °C. Gallium-rich condition was used to ensure enhanced surface diffusion. Gallium residues were etched by $FeCl_3$ after growths. In order to exfoliate the GaN epilayer, a Ni stressor (2.5 μm) with a Cr adhesion layer (30 nm) was deposited on the GaN surface which induces a mechanical strain at the GaN/2D material interface. Thermal release tape (TRT) was applied to the metal stressor/GaN multilayers, followed by lifting of the TRT from the substrate edge, resulting in mechanical exfoliation of the GaN nanomembranes with the metal stressors. The whole process is illustrated in Fig. S2.

  Poly-crystalline reference samples were obtained by growing GaN on 2D material/amorphous SiO_2, which is a poor growth substrate for GaN.

Fabrication of electronic modules in perforated e-skins

  We have utilized single-crystalline GaN nanomembranes (200 nm) fabricated by remote homoepitaxy processes as piezoelectric, wide bandgap semiconductor layers of strain sensors and UV sensors. For fabrication of single-crystalline GaN e-skins, we spin-coated and cured polyimide (PI) precursor, poly(pyromellitic dianhydride-co-4,4'-oxydianiline) in n-methyl-2-pyrrolidone from Sigma Aldrich, on Al/Ti (500 nm/20 nm)-coated, heavily-doped Si substrate (< 0.01 Ω cm) at 300 ºC for 1 hr. For the bonding, we used an epoxy resin (Fig. S8) with a glass transition temperature (T_g) higher than those of commonly used adhesives, such as polydimethylsiloxane (PDMS) and SU-8, to avoid the viscous behavior of adhesives at the curing temperature (> 250 ºC) of PI. Both sides of the substrate and GaN nanomembranes were treated with (3-Aminopropyl)triethoxysilane (APTES) solution in water (10 µL/20 mL) before bonding using a toluene solution of epoxy precursors made of 4,4'-methylenebis (N,N-diglycidylaniline) and 4,4'-diaminodiphenylmethane (both purchased from Sigma-Aldrich). After spin coating of the epoxy resin (1 μm) on the substrate, exfoliated GaN nanomembranes/Cr/Ni stressor multilayers on a handling elastomer consisting of styrene-ethylene/butylene-styrene, SEBS (Tuftec H1221 from AsahiKasei), and PDMS (Sylgard 184 from Dow Corning, base 10 : crosslinker 1) were placed on the uncured, sticky resin, and spatially uniform pressure was applied using a vise during curing of the epoxy resin at 150 °C for 1 hr to create a flat surface on the bonded region. The cured epoxy resin does not melt in the following high-temperature curing of PI. After the bonding, the elastomer holding the multilayers was detached in toluene and the Ni/Cr layers were removed by $FeCl_3$ solution and ammonium cerium (IV) nitrate (40 mg/mL, Sigma-Aldrich). The photoresist (AZnLOF2035, MicroChem) was patterned on the bonded GaN surface and NiN (20 nm) was deposited by reactive-sputtering under the flow of N_2 in order to form a Schottky contact on the exposed GaN surface for piezotronic strain sensors and UV sensors. It should be noted that the exposed GaN surface should be cleaned using HCl solution before the NiN electrode formation to form a good Schottky barrier. The subsequent Au (20 nm) deposition by e-beam evaporator and lift-off process resulted in interdigitated electrodes (IDEs) with 10 μm inter-spacing. On IDEs-deposited GaN, a thick photoresist (AZ10xt, MicroChem) was patterned as a mask to passivate

GaN active regions during dry etching (inductively coupled plasma, 5 mTorr, Cl_2 25 sccm, Ar 25 sccm, bias 70 W, plasma 500 W). APTES was treated again, and planarizing PI was spin-coated and cured at 300 ºC for 1 hr. The photoresist (AZnLOF2035, MicroChem) is once again patterned to deposit bottom antenna electrodes followed by e-beam evaporation of Ti (2 nm) and Au (100 nm) with a subsequent lift-off process. APTES was treated once more, and another layer of planarizing PI was spin-coated and cured at 300 ºC for 1 hr. The photoresist (AZ10xt, MicroChem) was patterned for a mask to etch away the PI layer (inductively coupled O_2 plasma, O_2 45 sccm, plasma 500 W) for electrical connection of IDEs on GaN active region and bottom antenna electrodes to metal interconnects which are to be deposited on top of the PI layer. After photoresist (AZnLOF2035, MicroChem) patterning, e-beam evaporation of Ti (2 nm), Au (100 nm), and Ti (5 nm) was conducted to form metal interconnects with auxetic dumbbell-hole patterns. The top PI layer (2 μm) was formed on the entire sample surface to locate electronic circuits near the neutral mechanical plane, thereby improving mechanical robustness. Note that some interfaces among layers were treated with APTES 1% v/v in deionized water to improve interface strength. Finally, after the PI layers are patterned by a photoresist (AZ10xt, MicroChem) and etched away (inductively coupled O_2 plasma, O_2 45 sccm, plasma 500 W), the fabrication of the auxetic dumbbell hole patterned electronic modules are completed. Whole processes are illustrated in Fig. S4 with corresponding optical microscopy images in Fig. S5.

Perforated e-skin fabrication

For the integration of the electronic modules to the auxetic dumbbell-hole patterned PDMS adhesives (SYLGARD 184, Dow Corning), detachment of the electronic modules from the Al/Ti/Si wafer by electrochemical lift-off process (dissolution of Al layer) was the first step. Before the lift-off process, the electronic modules were attached to TRT. Between modules and TRT, 2-μm-thick poly(methyl methacrylate) (PMMA) layer was inserted. After electrical wiring at the backside of the Si substrate, the samples were dipped into sodium chloride solution (0.9% NaCl) together with Pt wire as a counter electrode. As 1.8 V was applied to the Si wafer, the Al was dissolved in NaCl solution and electronic modules were transferred to the TRT accordingly. In order to form auxetic dumbbell-hole patterns on the electronic modules and the PDMS adhesives, Si mold-based soft lithography processes were utilized (see Supplementary Fig. S6). Firstly, a dumbbell-shaped Si mold (~20 μm depth) was prepared by deep reactive-ion etching (DRIE). After spin-coating of off-stoichiometric PDMS gels (40:1 weight ratio of PDMS pre-polymer: curing agent) on the Si mold, the electronic modules with TRT were placed on the uncured PDMS. Semi-transparency of the TRT allowed us to align the auxetic dumbbell mesh of the electronic circuits with the Si mold. After the alignment, the PDMS layer was cured at 80 °C with a constant pressure (1.29 kPa) to maximize the yield of the through-hole formation in the e-skin. After PDMS curing, the Si mold was separated from the samples. Note that the Si mold was treated with trichloro(1H, 1H, 2 H, 2H-perfluorooctyl)silane to reduce the Si surface energy, while APTES treatment was conducted on the surface of the electronic modules right before placing onto the uncured PDMS adhesives. Thus, the interface strength between the electronic modules and PDMS adhesive is much stronger than Si mold/PDMS interface strength, and such interface engineering processes facilitated the transfer of PDMS adhesives to the electronic modules without notable damage. After aligned bonding with the perforated electronic modules and the perforated PDMS adhesives, the TRT was detached by heating at 150 °C and the samples were dipped into acetone to remove PMMA. As the PMMA layer was dissolved, the perforated e-skin is produced.

The perforated e-skin was scooped from acetone using cellulose wipers (TX2009, Texwipe) and cleaned with IPA. After drying the perforated e-skin on the wipers, the edge of the perforated e-skin was attached to a temporary tattoo paper (Silhouette) which acts as a temporary handling layer (see Supplementary Fig. S7).

Preparation of skin replica

Dragon Skin silicone (1:1 ratio of part A to part B by weight; Dragon Skin 30; Smooth-On, Inc.) was poured on the forearm, allowed to cure for ~1 hr at room temperature, removed from skin, and placed in a Petri dish with the skin-textured side facing upward. Pouring Ecoflex (1:1 ratio of part A to part B by weight; Ecoflex 30; Smooth-On, Inc.) into the Petri dish, letting it cure at room temperature for ~12 hrs, and peeling it away yielded the skin replica samples made of Ecoflex.

GaN film characterization

The structural properties of GaN thin films were characterized by using a Bruker D8 high-resolution X-ray diffraction (XRD). Surface morphologies of GaN thin films were measured by using a Zeiss Merlin scanning electron microscope (SEM) and by using a Park NX10 atomic force microscope (AFM). For dislocation density determination, GaN thin films were etched in phosphoric acid at 160 ºC for 0.5 h. For transmission electron microscopy (TEM), the cross-sectional specimens were extracted from the GaN thin film by a lift-out technique in a dual-beam focused ion beam (FIB)/SEM (Helios G4, Thermo Fisher Scientific, U.S.). Prior to the ion-milling in a FIB/SEM, layers of carbon were deposited on the sample surface to protect the sample. The inner structures of single-crystalline GaN were observed using an aberration-corrected TEM (ARM-200F, JEOL, Japan) on the cross-sectional specimens at an acceleration voltage of 200 kV. The microscope is equipped with an aberration corrector in the objective lens (image corrector) and a Gatan OneView camera.

Evaluation of ultraviolet (UV) light sensing performance

UV conformal photocurrent microscopy (UVCPM) system was established to assess the UV sensing performance of single-crystalline GaN and polycrystalline GaN, (see (*13*) for details of the UVCPM system). The output currents from sensors were recorded with varying biases and illumination intensity by the Agilent B1500A semiconductor device parameter analyzer.

Measurement of surface acoustic wave (SAW) e-skin

A handheld low-cost open hardware vector network analyzer (VNA), NanoVNA H4, or a tabletop laboratory VNA, Agilent N5230A VNA (as a comparison to NanoVNA), were used for measurements of SAW devices (Fig. S9). A magnet wire made of a metal wire covered with very thin insulation was used to build a reader antenna. The reader antenna was connected to the VNA. Dumbbell-shaped Ti/Au/Ti (2 nm/100 nm/ 5 nm) electrodes were used to build a stretchable antenna and a stretchable interconnect between the stretchable antenna and a GaN SAW device. The reader antenna was wirelessly coupled with the stretchable antenna on the GaN SAW e-skin sensor tag. The maximum data rate achieved by the measurement system was approximately 31.39

Hz. The distance between the reader antenna and the GaN SAW e-skin sensor tag was about 1 mm for wireless pulse and UV measurement and was around 2 mm for wireless ion sensing.

Evaluation of wireless UV sensor performance

GaN SAW e-skin was fabricated as written above. GaN SAW e-skin had hole patterns etched through the top PI layer to expose the GaN surface to UV light. UCVPM system mentioned above was used, and the output signals upon irradiation of UV light with varying intensities (24.65 $\mu W/cm^2$, 65.64 $\mu W/cm^2$, 256.2 $\mu W/cm^2$, 403.4 $\mu W/cm^2$, 671.0 $\mu W/cm^2$, and 898.5 $\mu W/cm^2$) were recorded by VNA.

Fabrication and evaluation of ion sensing performance

GaN SAW e-skin was fabricated as written above. The GaN SAW e-skin had hole patterns etched through the top PI layer. On top of either GaN SAW e-skin or quartz crystal microbalance (QCM), ion-selective membrane (ISM) solutions in tetrahydrofuran (Fig. S19 and Table S2) were spin-coated at 3000 rpm. The solution is highly viscous so that it does not spread all over the skin e-skin unless the solution is fully dispersed before spin-coating. The ISM was dried at 80 ºC for 5 min. The resulting GaN SAW e-skin ion sensors and QCM ion sensors were tested using Agilent N5230A vector network analyzer and Biolin Scientific Q-Sense E4 system, respectively. NaCl solutions containing different Na^+ ion concentrations were pumped over the e-skin using peristaltic pumps at a flow rate of 0.184 mL/min. Alternating injections of 0.86 mM NaCl solution and distilled water over the device yielded the wireless recordings in Fig. 4C. To obtain the calibration curve in Fig. 4D, output signals were collected by SAW e-skin sensor exposed to varying concentrations of Na^+ ions (0.86 mM, 2.71 mM, 8.56 mM, 14.92 mM, 27.05 mM, 34.22 mM, and 85.56 mM) for 5 min each. The collected data were time-averaged and plotted as a function of the Na^+ ion concentration.

Calculation of strain energy and work of adhesion for the critical thickness of delamination

To avoid mechanical failure with securing its conformability on the e-skin, one of the most crucial features that must be considered is the maximum allowable thickness of rigid GaN membranes on soft human skin. To wrap curvilinear skin surface, work of adhesion of e-skin need to be higher than strain energy of e-skin. As shown in Fig. 1B, the strain energy of GaN e-skin sensors is significantly increased by GaN thickness. The bending-induced strain energy per area of the e-skin device is (*32*):

$$\frac{U}{A} = \frac{E'' \, t^3}{24 \, R^2}$$

where U is bending-induced strain energy, A is an area of the device, E" is the effective elastic modulus of the device, t is the thickness of the device, R is the radius of curvature. R was assumed to be about 1 mm for skin (*33*). The work of adhesion at the sensor region is 2.9 N/m (*13*). We chose the work of adhesion of non-patterned PDMS because we are considering microscopic conformability, not macroscopic conformability. Our device consists of multiple layers: layer 1 (l_1), layer 2 (l_2), layer (l_3), and so on. Thus, its effective elastic modulus, E", was calculated using the formula (*34*):

5

$$E'' = \sum_{k=1}^{n} E_{l_k} \frac{t_{l_k}}{t}$$

where E_{lk}: Elastic modulus of layer k, t_{lk}: thickness of layer k, and n is the total number of device layers.

The critical thickness, at which the strain energy within the film exceeds the work of adhesion, is estimated to be 300 nm (Fig. 1B). In other words, the maximum allowable GaN thickness for the conformal contact is estimated to be 300 nm. Thus, it is essential to maintain GaN thickness less than 300 nm to follow the skin activity and adhere to the e-skin without delamination.

COMSOL Multiphysics simulation

Finite element analysis of the SAW device was done using COMSOL Multiphysics. The geometry was drawn in 2D (Fig. 2E). The interdigital transducer (IDT) electrodes were periodic with a length of 10 µm, a spacing of 10 µm, and a period of 40 µm. The thickness of IDT electrodes was 40 nm, and the width of IDT electrodes in the direction orthogonal to the 2D drawing plane was 268 µm. GaN thickness was varied. The thickness of the top PI was 760 nm, and the thickness of the bottom PI was 1.72 µm. The bottom sapphire was set to be 120 µm, which is 3 times the period of SAW. We obtained elasticity matrix and coupling matrix values of GaN from (*18*, *35*). We used Solid Mechanics and Electrostatics physics interfaces. The upper boundary of the top PI and the lower boundary of the bottom PI were set to be free boundaries. The lower boundary of the bottom sapphire was fixed. The periodic conditions were applied to the left and right boundaries of the drawn 1 period of geometry. All the geometry was under mechanical damping, and the piezoelectric domain had additional conduction loss. The two electrodes functioned as ground and terminal. Frequency domain analysis was used to calculate the conductance, $G = Re(Y)$, and the susceptance, $B = Im(Y)$, between the two electrodes. We calculated the electromechanical coupling coefficient (k^2) using the equation, $k^2 = \frac{\pi}{4N}\left(\frac{G}{B}\right)_{f=f_r}$, where N and f_r are the number of IDT finger pairs and resonant frequency, respectively.

Simulation of power consumption of GaN SAW sensors (Ansys HFSS Finite Element Analysis)

During wireless measurement, the power is radiated from the reader coil (P_r). The radiated power (P_r) is consumed as free-space path loss (FSPL) as it propagates from the reader coil to a SAW sensor tag. Then SAW sensor tag receives the incident power through a SAW tag coil. There is an ohmic loss in the SAW tag coil ($P_{tag\ coil}$) in the receiving process. The received power is delivered to the SAW sensor and finally consumed (P_{SAW}). This process is illustrated in Fig. S13A. The following relations between the power consumption of each component are valid:

(Radiated power from reader coil, P_r) = (Free-space path loss, FSPL)
+ (SAW tag coil loss, $P_{tag\ coil}$)
+ (SAW sensor power consumption, P_{SAW})

Based on the measured impedance values of SAW devices (Fig. S13B) as well as the dimensions of the reader and SAW tag coils, we can calculate and plot the power consumption of each component, using Ansys HFSS finite element analysis (FEA) (Fig. S13C).

For details on the Ansys HFSS FEA simulation, the reader coil was set to port 1, and the SAW tag coil to port 2. For port 2, an experimentally measured impedance of the SAW device was used as the source impedance, and no power source was connected. Port 1 was supplied with input power. The calculated reader coil inductance was in agreement with the measured inductance value of the reader coil.

Both the reader coil and the SAW tag coil have power consumption. Coil metals have a finite conductivity, and the electric fields induce surface currents on the surfaces of the coil metals. These surface currents lead to ohmic loss and power consumption in the coils. The coil power consumptions were calculated by the integration functionality of Ansys HFSS FEA simulations:

$$\int (surface\ loss\ density) \cdot (coil\ surface\ area) = (power\ consumption\ in\ coil)$$

The radiated power from the reader coil, P_r, was calculated using the "compute antenna parameters" function in Ansys HFSS. The power delivered to port 2 models the power consumption of the SAW device. The free-space path loss, FSPL, was obtained by subtracting the SAW sensor tag power consumption (= SAW tag coil loss, $P_{tag\ coil}$ + SAW device power consumption, P_{SAW}) from the radiated power from the reader coil, P_r.

Fig. S13D shows the plot of calculated power consumption levels of each component as functions of reader coil-to-SAW sensor tag coil distance. As the distance between the coils increases, the delivered power to the SAW sensor decreases. From the reader side, the delivered or reflected power to the SAW sensor can be monitored over the frequency range. The change in the reflected power over the frequency range is used as sensor signals by the reader. These sensor signals are roughly proportional to the power consumption of SAW sensor and are one to two orders of magnitude smaller than the power consumption of SAW sensor.

For the given noise amplitude, the SAW sensor signal output determines the readability of sensor signal. The signal-to-noise ratios (SNRs) of SAW sensor tag outputs were measured (Fig. S17) to determine the minimum required SAW sensor signal output. The SAW sensor signal output is determined by the power consumption of SAW sensor. The power consumption of SAW sensor when the SNR is equal to 3 is the minimum required power for SAW sensor tag (=$P_{tag\ coil}$ + $P_{SAW,\ min}$). The minimum required SAW sensor tag power was multiplied by the sampling interval to obtain the energy consumption of each measurement, i.e. 3.7684 nJ.

Supplementary Text

Advantages of remote epitaxy and two-dimensional material-based layer transfer (2DLT)

Remote epitaxy can yield single-crystalline GaN membranes with <300 nm thickness because it directly seeds from the substrate and produces ultrathin epitaxial membranes that can be released from the 2D materials. This process also reduces material cost for GaN films by allowing the re-use of costly epitaxial substrate via a simple oxygen plasma etching process followed by the growth of another 2D layer.

Device structure of GaN SAW sensors.

Freestanding GaN on PDMS skin patch was achieved by transferring the SAW device onto PDMS patch such that the devices are aligned on top of the holes that penetrate through the patch. The SAW device is electrically connected via stretchable interconnects to a stretchable antenna. Dumbbell-shaped holes patterned throughout the patch ensure the stretchability, conformability, and breathability of our e-skin (13).

Mechanism and signal conversion flow in wireless GaN SAW sensors

When an external wireless reader initiates electromagnetic (EM) waves, the stretchable antenna converts them into electrical signals. Patterns of interdigitated metal electrodes (NiN$_x$/Au, 20/20 nm) deliver electrical energy from the antenna (Ti/Au, 2/100 nm) to GaN device (size: 408 μm × 640 μm, thickness: 200 nm), which serves as piezoelectric resonator that converts the electrical signal to SAW. SAW is sensitive to changes in mechanical strain and mass (due to absorption/desorption of ions, e.g.), as well as ultraviolet (UV) exposure (due to optical absorption by GaN). SAW is then converted back into electrical signal and transmitted back through the antenna. The changes in the resonant frequency of the electric signal yield information about the mechanical, optical, and biochemical stimuli detected by the GaN SAW sensor.

Wireless GaN SAW UV sensors

Holes are patterned through the polyimide coating to expose the GaN sensor to UV radiation (Fig. S22). Absorption of UV light leads to variation in the electrical conductivity of GaN SAW device, which in turn alters its patterns of acoustic wave generation. Calibration data in Fig. 4G shows the sensor response to varying UV intensities (see Methods for detailed procedures).

Langmuir-Freundlich isotherm fitting model for ion concentration and output

Langmuir isotherm model interprets adsorption and desorption of target molecules in relation to the limited number of adsorption sites and the equilibrium constant. Freundlich isotherm model takes heterogeneous surface into account to consider multi-adsorption sites. The combination of these two models is the Langmuir-Freundlich isotherm model, expressed by the formula (36):

$$Q = \frac{Q_{total} \times K \times c^n}{1 + K \times c^n}$$

where Q is the number of occupied adsorption sites, Q_{total} is the total number of adsorption sites, K is the equilibrium constant, c is the ion concentration, and n is the coefficient that represents the

heterogeneity of the surface ranging from 0 (heterogeneous) to 1 (homogeneous). Since our ion-selective membrane is composed of a single substance, we can assume the surface of our GaN SAW-based device as homogeneous (n = 1). As a result, Langmuir-Freundlich isotherm fitting was successfully conducted as shown in Fig. 4D with an R^2 value of 0.984 ($Q_{saturation}$ = 0.5921 ± 0.0482 and K = 0.0301 ± 0.0053). The data points used for the fitting were acquired at room temperature.

Wireless communication distance of GaN SAW sensors
        For the readable signal (SNR > 3), the following condition should be met:
        SAW sensor tag power consumption (= $P_{tag\ coil}$ + P_{SAW})
                ≥ Minimum SAW sensor tag power consumption (= $P_{tag\ coil}$ + $P_{SAW,\ min}$)
or
        (Radiated power from reader coil, P_r) - (Free-space path loss, FSPL)
                ≥ Minimum SAW sensor tag power consumption (= $P_{tag\ coil}$ + $P_{SAW,\ min}$).
        Please refer to Fig. S13A for the definitions of each term. As the wireless communication distance d increases, FSPL increases. In order to have a long wireless communication distance (d), either radiated power from reader coil (P_r) should be large or minimum SAW sensor tag power consumption (= $P_{tag\ coil}$ + $P_{SAW,\ min}$) should be small.
        Because of safety concerns, the radiated power (P_r) cannot be increased indefinitely. For the given the P_r, the SAW sensor tag power consumption decreases with an increase in FSPL. The minimum required power consumption of the SAW sensor tag (=$P_{tag\ coil}$ + $P_{SAW,\ min}$) determines the longest wireless communication distance d.
        For our electrically-small near-field coil antennas (antenna coil circumference << a wavelength of electromagnetic waves at the operating frequency), the FSPL increases rapidly beyond the distance equal to the diameter of the coils, which means our electrically-small coil antennas cannot be used for longer distance communication.
        Our SAW sensor tag can be connected to conventional far-field antennas, such as a full wavelength loop antenna, for long-distance communications. For conventional far-field antennas, FSPL is proportional to $1/d^2$,

$$(\text{Free-space path loss, FSPL}) \propto \frac{1}{d^2}$$

where d is the distance between the reader antenna and the SAW sensor tag antenna. For the constant radiated power from a reader antenna (P_r), low sensor tag power consumption (=$P_{tag\ coil}$ + P_{SAW}) allows high free-space path loss, leading to longer range wireless communication. Our SAW sensor tag has very low power consumption. A near-field coil antenna in our SAW sensor tag, not our SAW device, limits the wireless communication range. We can replace the near-field coil antenna with a far-field loop antenna for future long-range wireless SAW e-skin.

Comparison of communication distance and power consumption between chip-based and chip-less e-skins
        The operating distances of near-field communication (NFC) chip-based wireless sensors are 2-3 cm when using standard NFC-equipped smartphones, and 20-30 cm using a 30 cm x 30 cm antenna (power: 4 W). (*37-40*) The communication range becomes larger with antenna size and radio-frequency (RF) power. NFC chip requires inductive power transfer, which limits the communication distance to the coil diameter. On the other hand, radio-frequency identification

(RFID) can either work through inductive coupling (similar to NFC) or work over a long distance (> 1 m) by the combination of far-field and backscattering operations (*10*). Our SAW devices currently have a similar wireless communication distance to that of NFC chips.

However, the communication range of our SAW devices can be extended to > 1 m by re-designing our antenna for far-field and backscattering operation (similar to RFID backscattering operation). This type of far-field and backscattering wireless SAW sensor has been demonstrated in non-freestanding SAW sensors that are tethered to wafers. (*41*)

In the case of NFC, powers are delivered through inductive coupling and the alternating current (AC) power is converted to direct current (DC) voltage to supply circuits inside the NFC chip. On the hand, SAW is a passive backscattering type. The reader sends electromagnetic waves to a SAW device and reads reflection coefficients at a frequency range. The reflected signals at the frequency range are monitored to find the resonant peak of the SAW device. The interrogation signal for the reading of the reflection signal should be sufficiently higher than the noise background. The power consumption of our SAW devices is a portion of the interrogation signal from the reader that is consumed inside our SAW devices.

SAW sensor tag consumes lower power for operation than chip-based technologies (Fig. 3D). The power consumed by an NFC chip-based sensor is 4 mJ per measurement (*42*). In contrast, we have estimated the power consumption in our SAW sensors as illustrated in Fig. S13 (the details of the simulation methods appear in the Method section). For the coil-to-coil distance of 14 mm, our SAW sensor (blue line in Fig. S13) consumes power of ~ 4 nJ per measurement, which is orders of magnitude smaller than that of NFC-based systems.
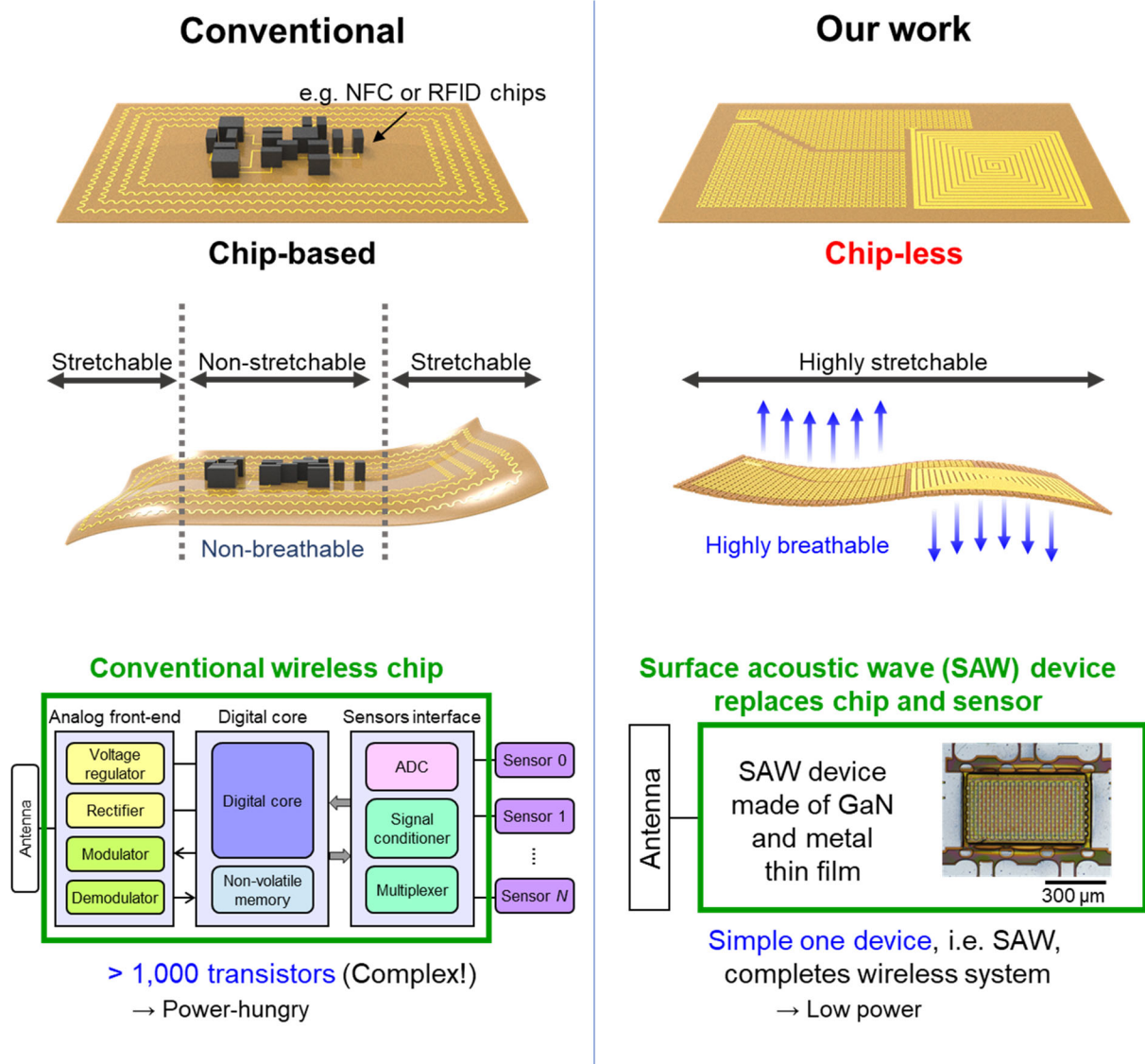
Fig. S1. Comparison between conventional chip-based wireless e-skin and chip-less wireless e-skin in this work. For conventional e-skins, chips are crucial for converting analog signals from the sensors to digital signals and sending them through the antenna wirelessly.
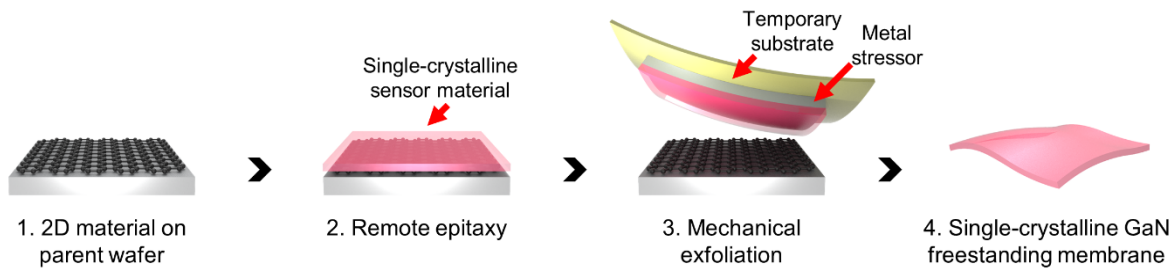
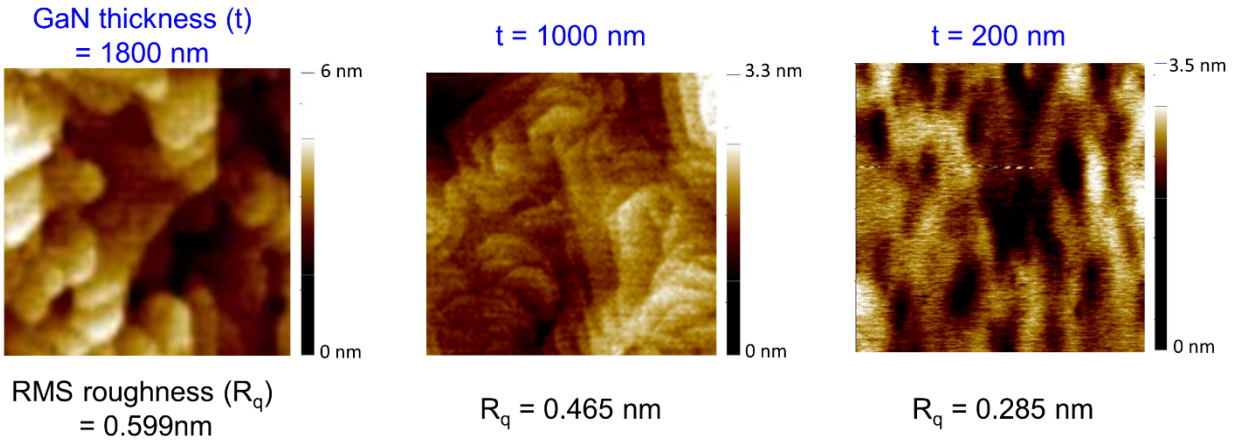**Fig. S2.** Schematic illustrations for the production of GaN nanomembranes via remote homoepitaxy.

GaN thickness (t)
= 1800 nm

t = 1000 nm

t = 200 nm

RMS roughness (R_q)
= 0.599nm

R_q = 0.465 nm

R_q = 0.285 nm

Fig. S3. Atomic force microscopy images of GaN with different thicknesses (1800, 1000, and 200 nm). The size of images is 1 μm × 1 μm.

1. Ti/Al deposition on Si wafer

2. Bottom PI coating
(1.32 μm)

3. Single-crystalline GaN
bonding using epoxy

4. IDEs (NiN$_x$/Au) deposition

5. Mask patterning before etching

6. Dry etching

7. Remove etch mask

8. Bottom PI re-coating
(0.76 μm)

9. Antenna (Ti/Au) deposition

10. Middle PI coating
(2.7 μm)

11. PI opening by
dry etching

12. Interconnect (Ti/Au/Ti)
deposition

13. Top PI coating
(0.76 μm)

14. Dumbbell-hole pattern
by dry etching

15. Electrochemical release

16. PDMS adhesive layer
using Si mold

Fig. S4. Schematic illustration showing the fabrication steps for GaN e-skins.

IDEs (NiN$_x$/Au) deposition on GaN

Dry etching and antenna deposition

PI opening by dry etching

200 µm

No pattern yet

200 µm

200 µm

No pattern yet

200 µm

200 µm

Interconnect deposition and top PI patterning

PDMS adhesive layer using Si mold

200 µm

200 µm

200 µm

200 µm

200 µm

200 µm
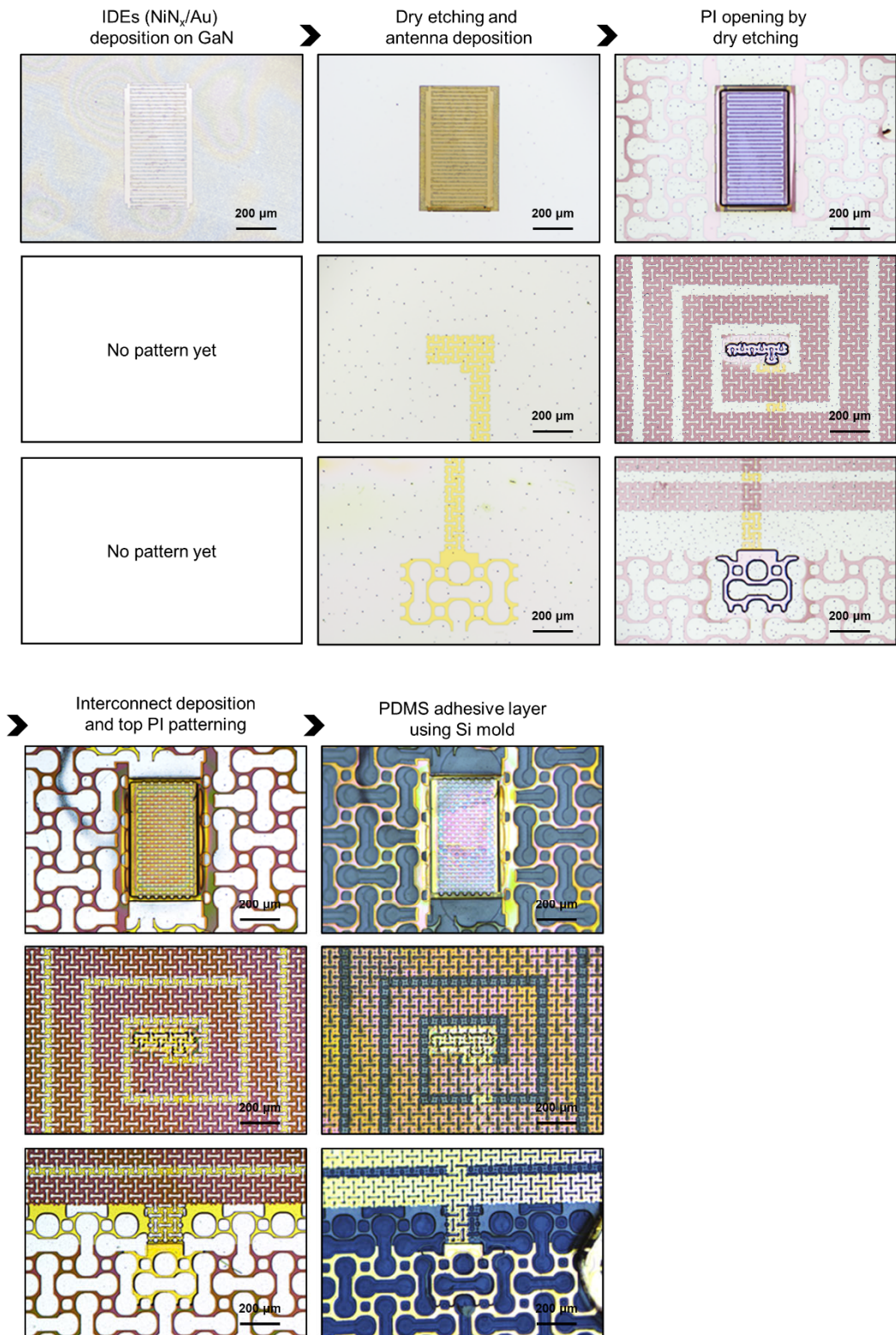
Fig. S5. Optical microscopy images from the fabrication process of GaN e-skins.

15

A. Si mold fabrication

A-1. Si wafer

A-2. Photolithography
Photoresist

A-3. Etch Si wafer (20 µm)
Deep reactive ion etching

A-4. Remove photoresist

A-5. Surface silane treatment
After O_2 plasma

A-6. PDMS spin-coating
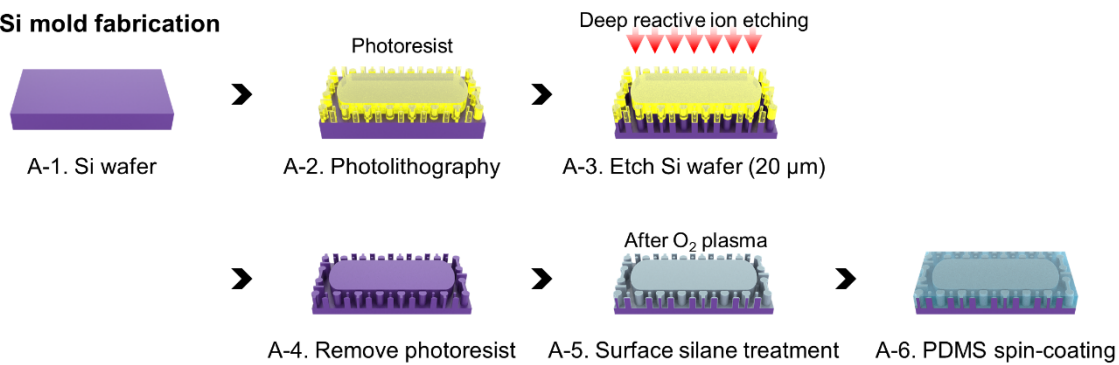
B. Electrochemical release of device

B-1. Fabricated device

B-2. PMMA spin-coating
PMMA

B-3. TRT attachment
Thermal release tape

B-4. Electrochemical release

C. PDMS bonding

C-1. Align and press
(A-6 + B-4)

C-2. Peel off from Si mold

C-3. Remove TRT at 120℃

C-4. Remove PMMA
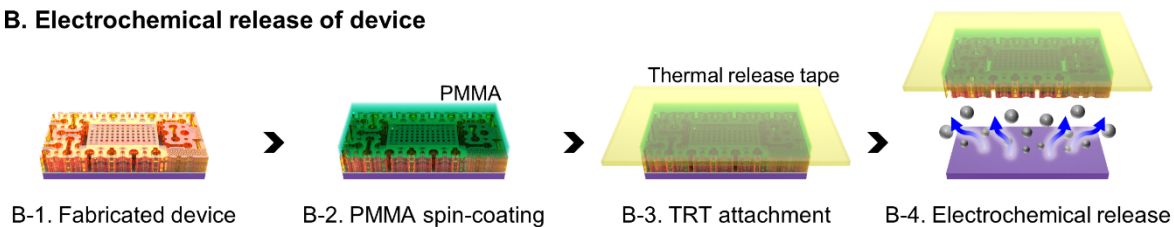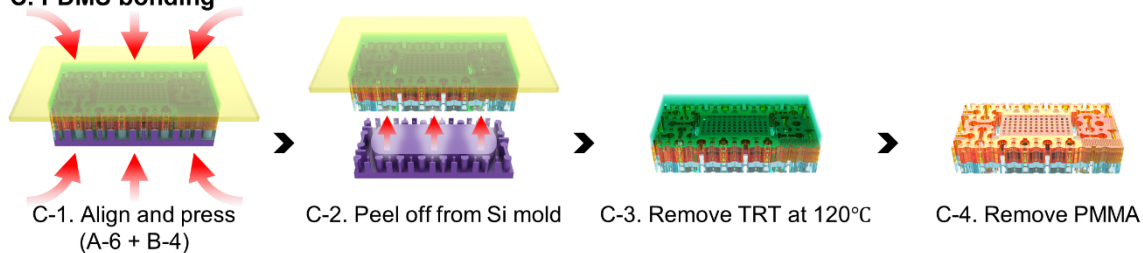
Fig. S6. Schematic illustrations of GaN e-skin fabrication.

Before electrochemical release

After electrochemical release

After tattoo sticker attachment

GaN device with metal electrodes
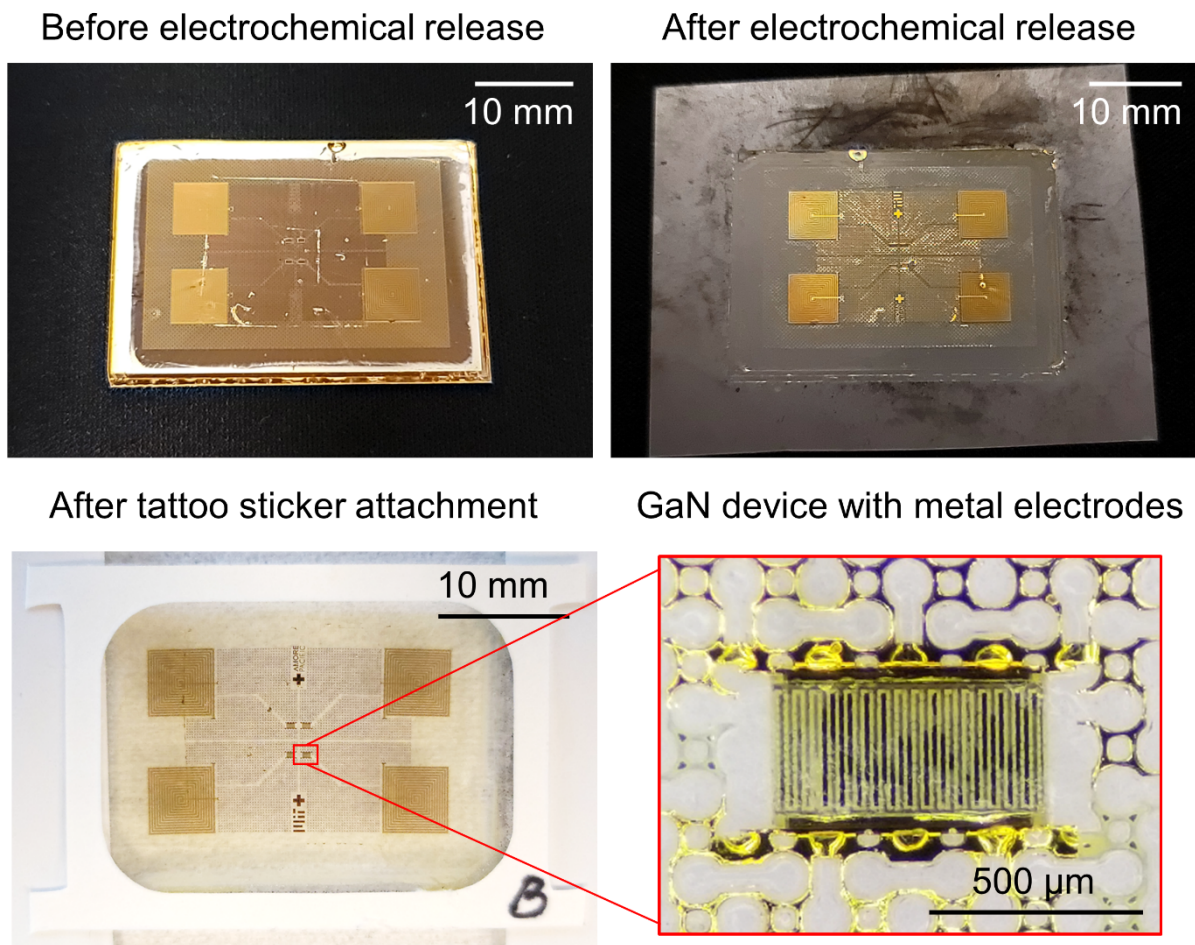
Fig. S7. Photographs of the fabricated GaN e-skin devices.
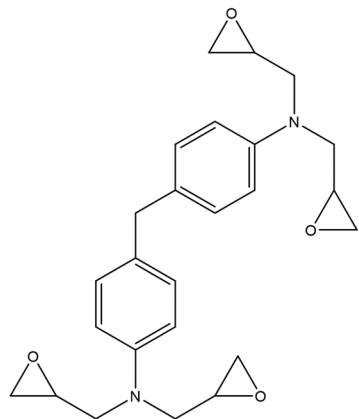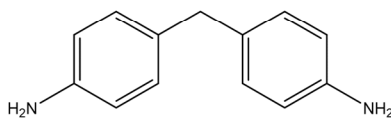
4,4′-Methylenebis(N,N-diglycidylaniline)   4,4′-Diaminodiphenylmethane

Fig. S8. Chemical structures of epoxy adhesive precursors. These epoxy adhesive precursors were dissolved in toluene and spin-coated on substrates. The toluene was removed at 110 ºC, and the adhesive precursors remained as liquid. The precursors were cured at > 150 ºC.
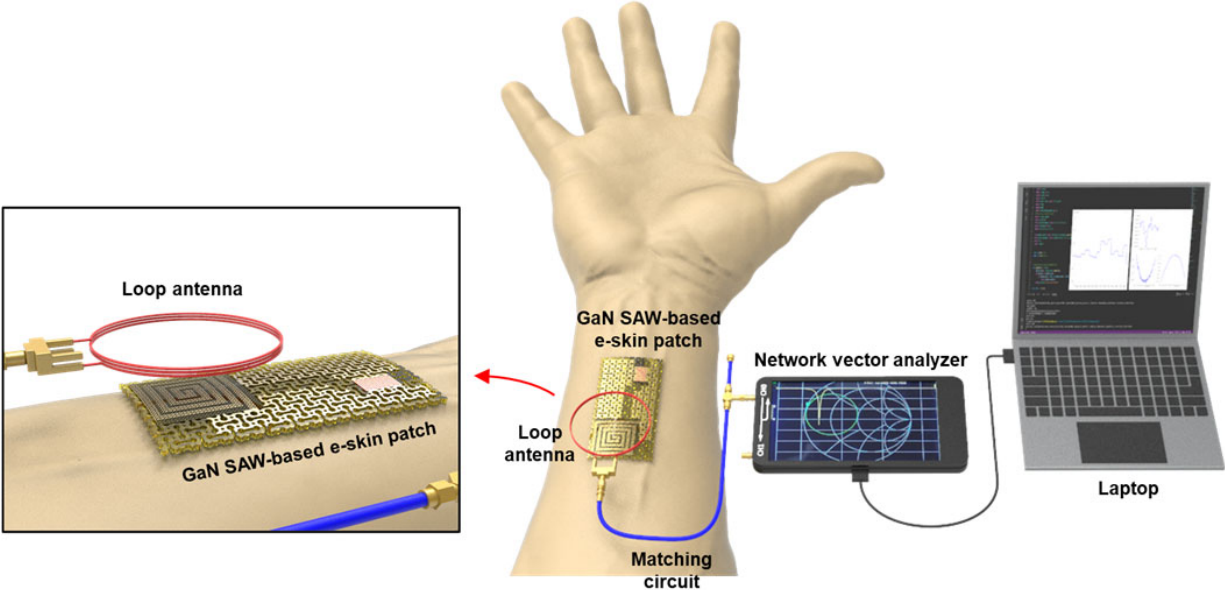
Fig. S9. Schematic illustrations of wireless e-skin measurement system.
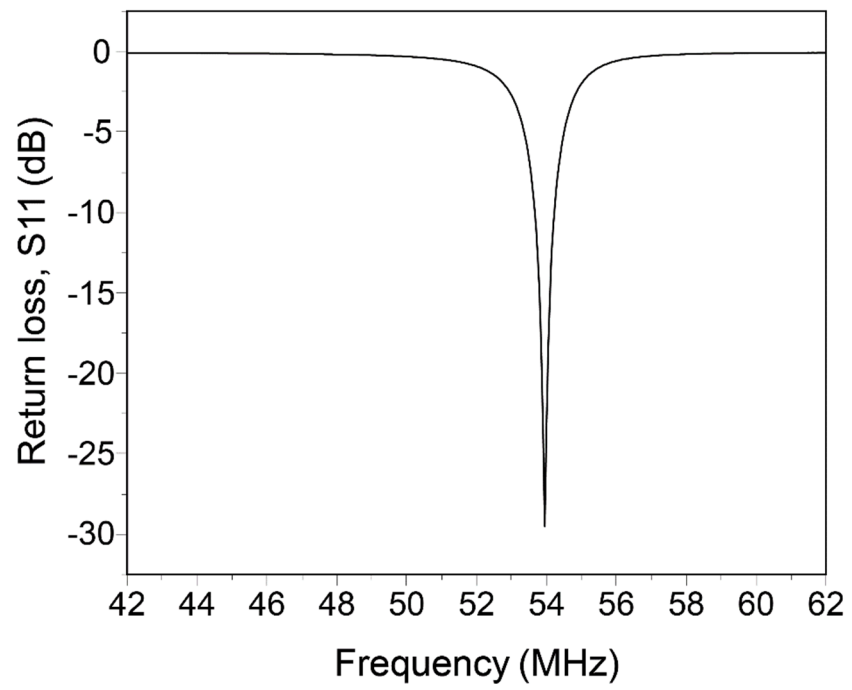
Fig. S10. Return loss (S_{11}) of our wireless measurement system.
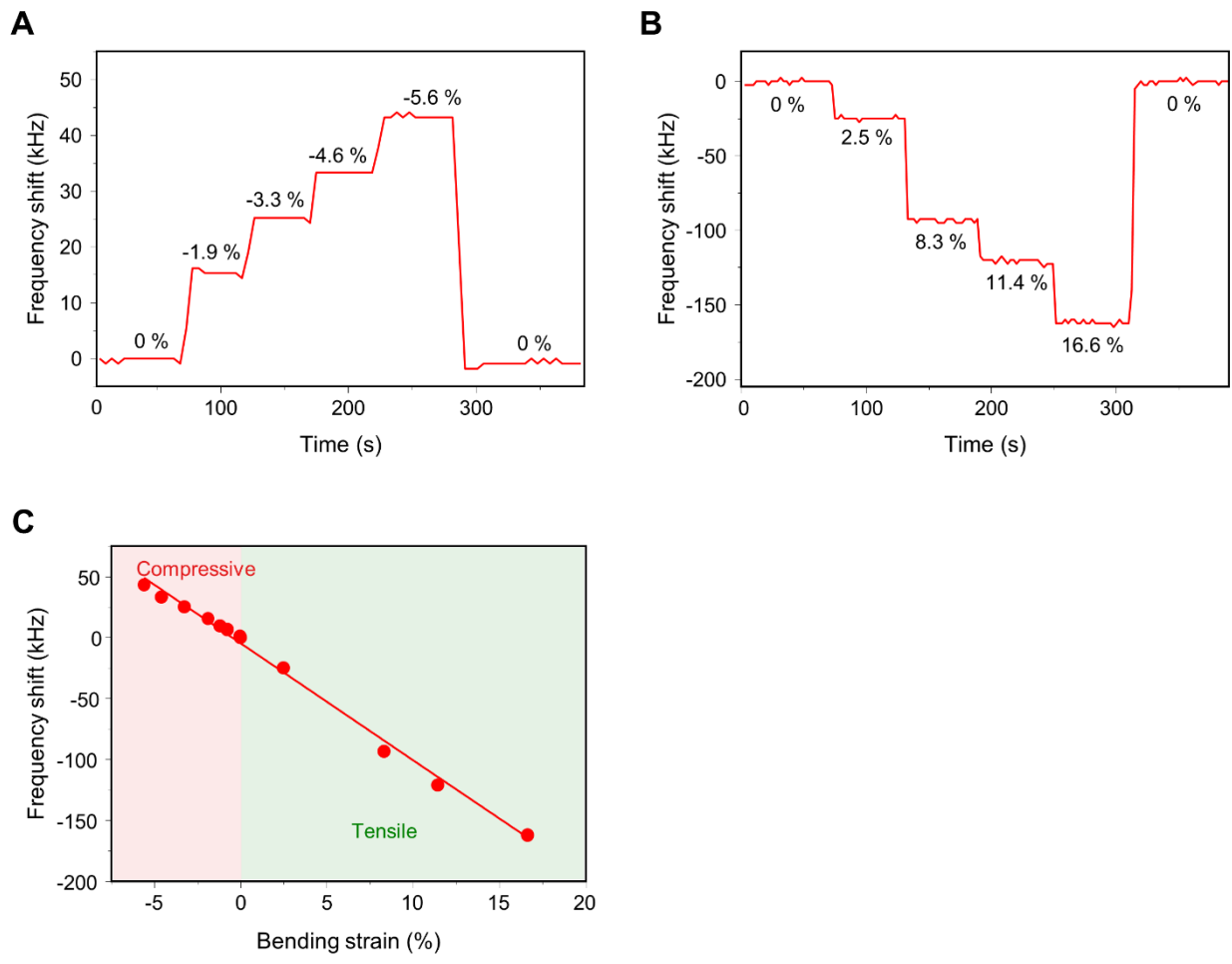
Fig. S11. Real-time output responses and characteristics of GaN surface acoustic wave (SAW) e-skin strain sensors under **(A)** compressive strain and **(B)** tensile strain. **(C)** Output response depending on strain.
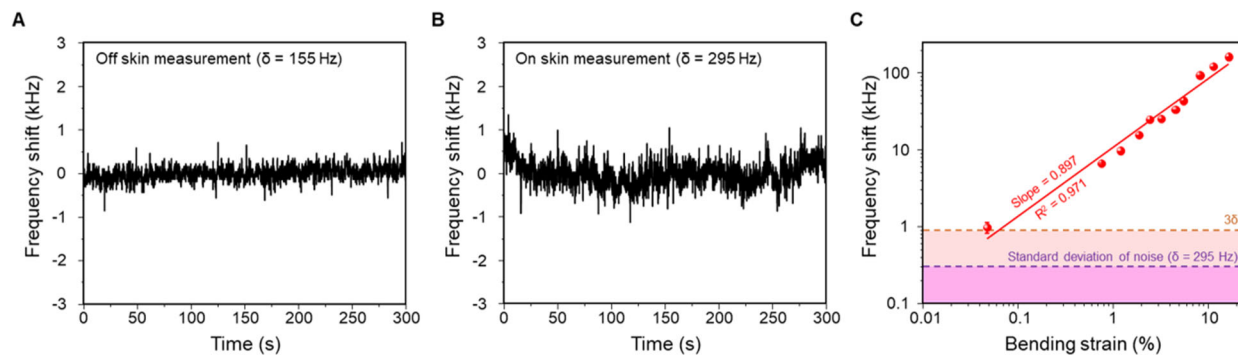
Fig. S12. Noise measurement and the minimum limit of detection of GaN SAW e-skin strain sensors. **(A-B)** Continuous wireless recording of the baseline noise in GaN SAW strain sensors placed (A) off-skin and (B) on-skin for 5 min. Standard deviation (δ) in the measured noise is 155 Hz and 295 Hz, respectively. **(C)** Linearity of frequency shift as a function of bending strain. The theoretical minimum limit of strain detection was calculated with 3δ, which was around ~0.05%.
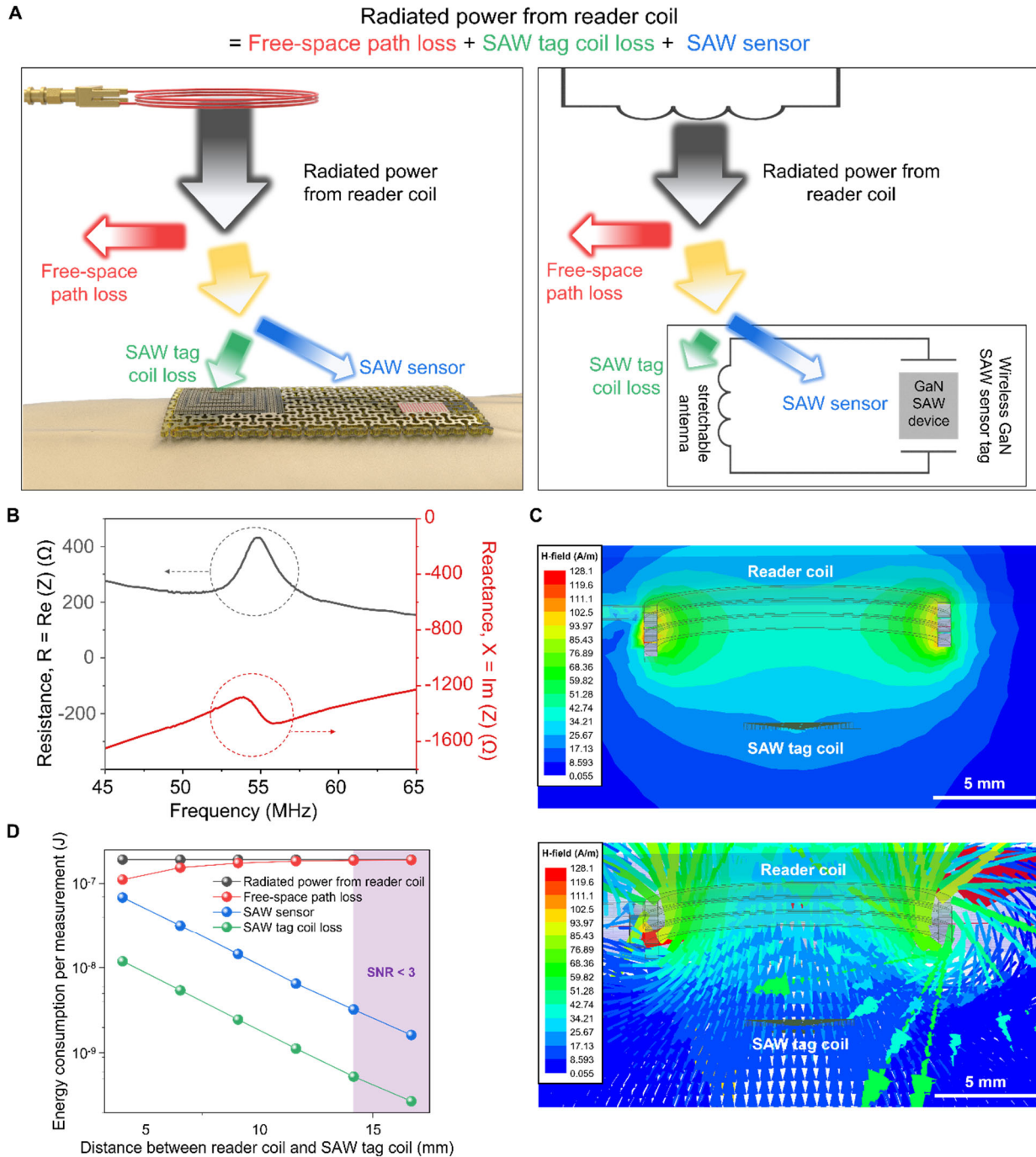
Fig. S13. Estimation of total power consumed during wireless measurement using an SAW sensor. (**A**) Schematic illustration of the total power consumption. Radiated power from reader coil is consumed as free-space path loss, SAW tag coil loss, and SAW sensor consumption. (**B**) Measured impedance ($Z = R + jX$, where Z, R, and X are impedance, resistance, and reactance, respectively) values of our SAW sensor which were used for power consumption calculation. (**C**) Simulated magnitude (top) and direction (bottom) of H field during wireless power transfer from reader coil to SAW tag coil, obtained using Ansys HFSS finite element analysis. (**D**) Estimation

of energy consumption per measurement for each component in (A) as functions of the distance between reader coil and SAW tag coil. Signal-to-noise ratio (SNR) value is from Fig. S17.
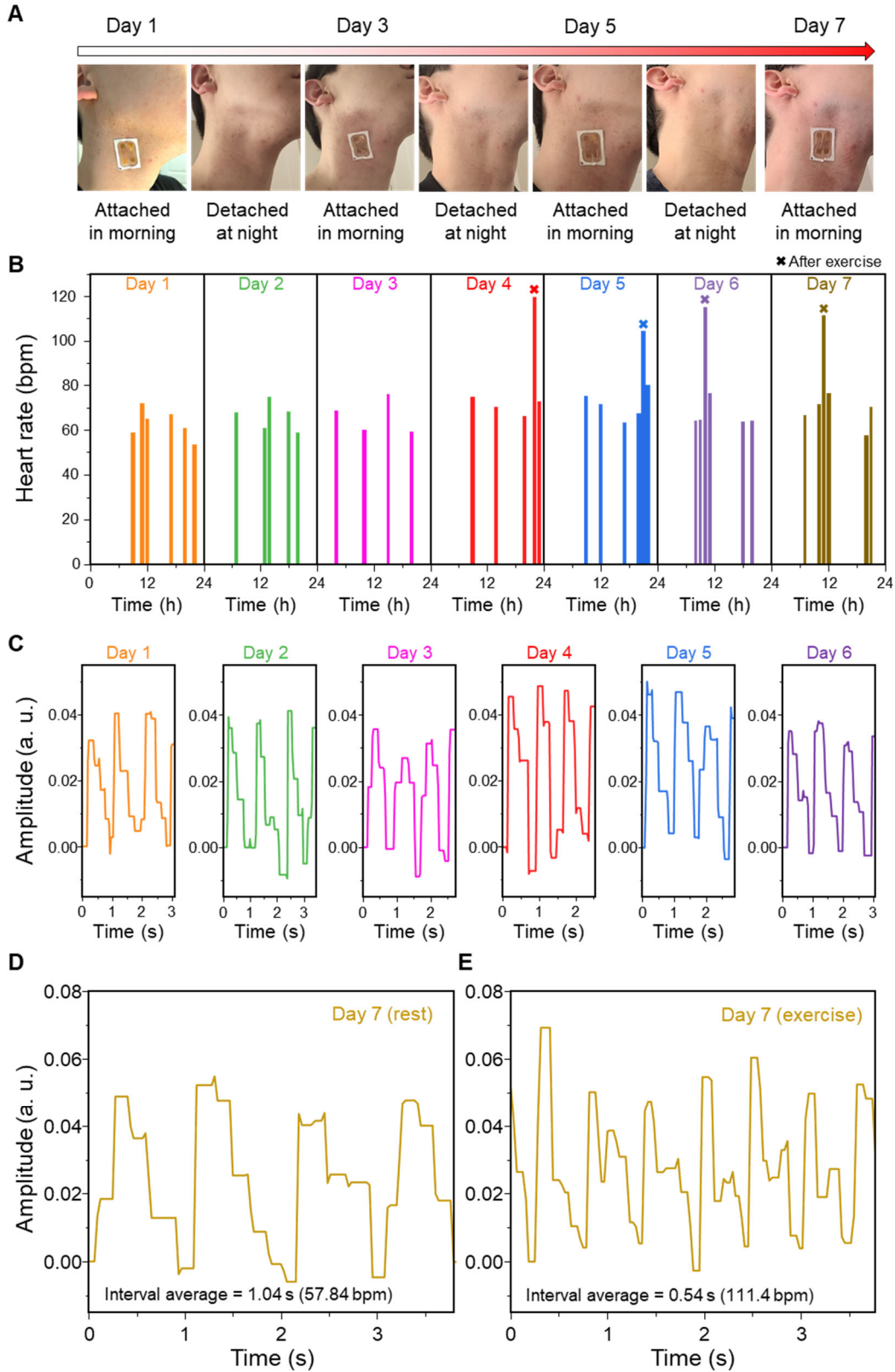
Fig. S14. Evaluation of reusability and long-term wearability of GaN SAW-based e-skin. (A) Photographs of an e-skin device attached on the neck area for pulse monitoring during daytime

over a period of a week. The same e-skin device was peeled off at night before sleep and re-attached in the morning (worn ~17 hrs per day) **(B)** Wireless recording of heart rate (beats per min, bpm) throughout the day over a period of 7 days. Normal range of pulse was 55-80 bpm, while after exercise it was 110-120 bpm ('×' mark; only on days 4-7). Changes in heart rate could be observed via pulse measurement following exercise (days 4-7). **(C)** Representative waveforms of the wirelessly recorded pulses for each day. **(D, E)** Wireless pulse measurement curves on Day 7 after (D) rest and (E) exercise, respectively.
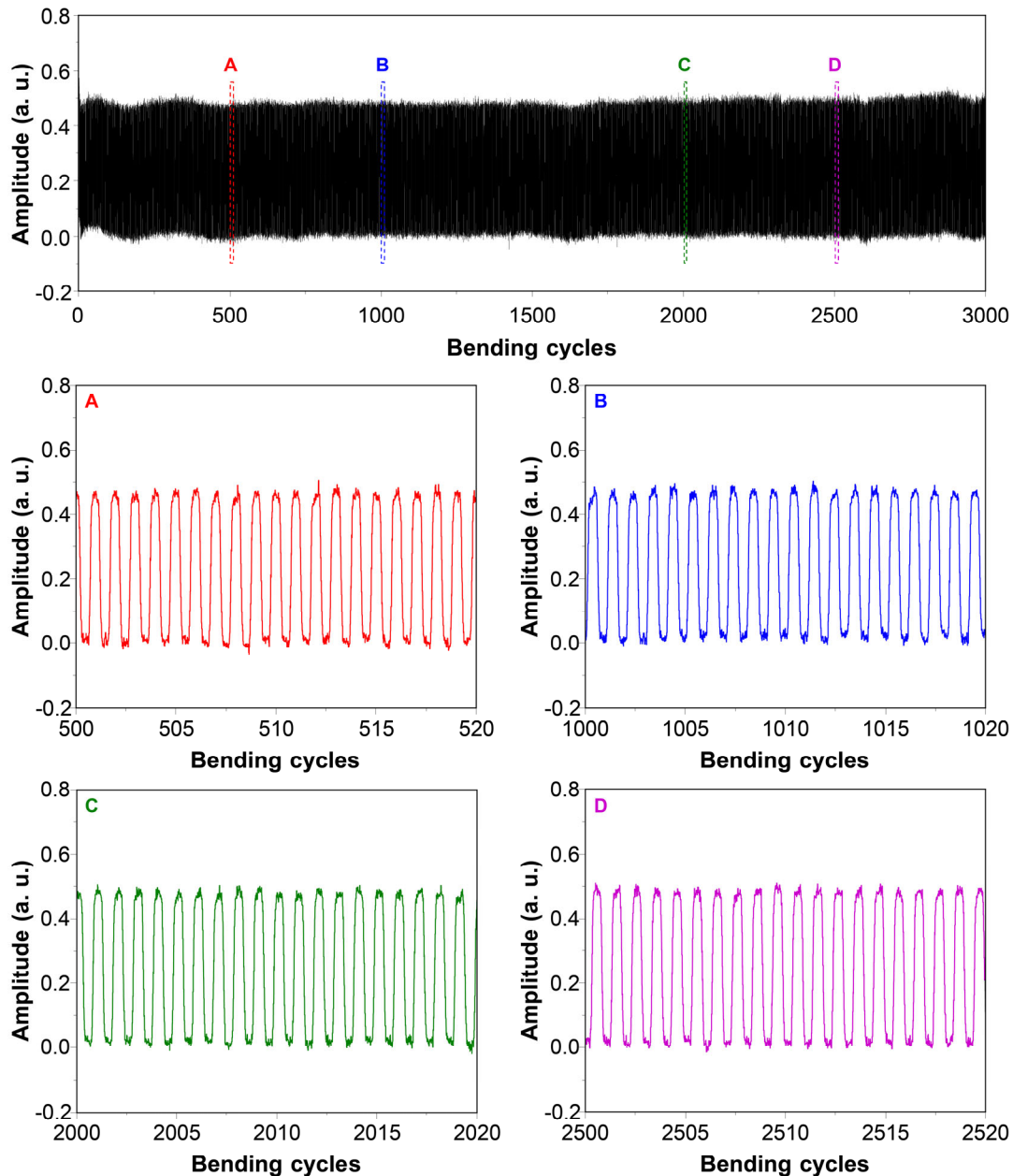
Fig. S15. Wireless recording of GaN SAW-based strain sensor during bending test. Continuous wireless recording from GaN SAW-based strain sensor on e-skin throughout 3000 bending cycles at a bending radius of 6.54 cm (top). Magnified waveforms of the strain profile at different time points (A-D) appear below.
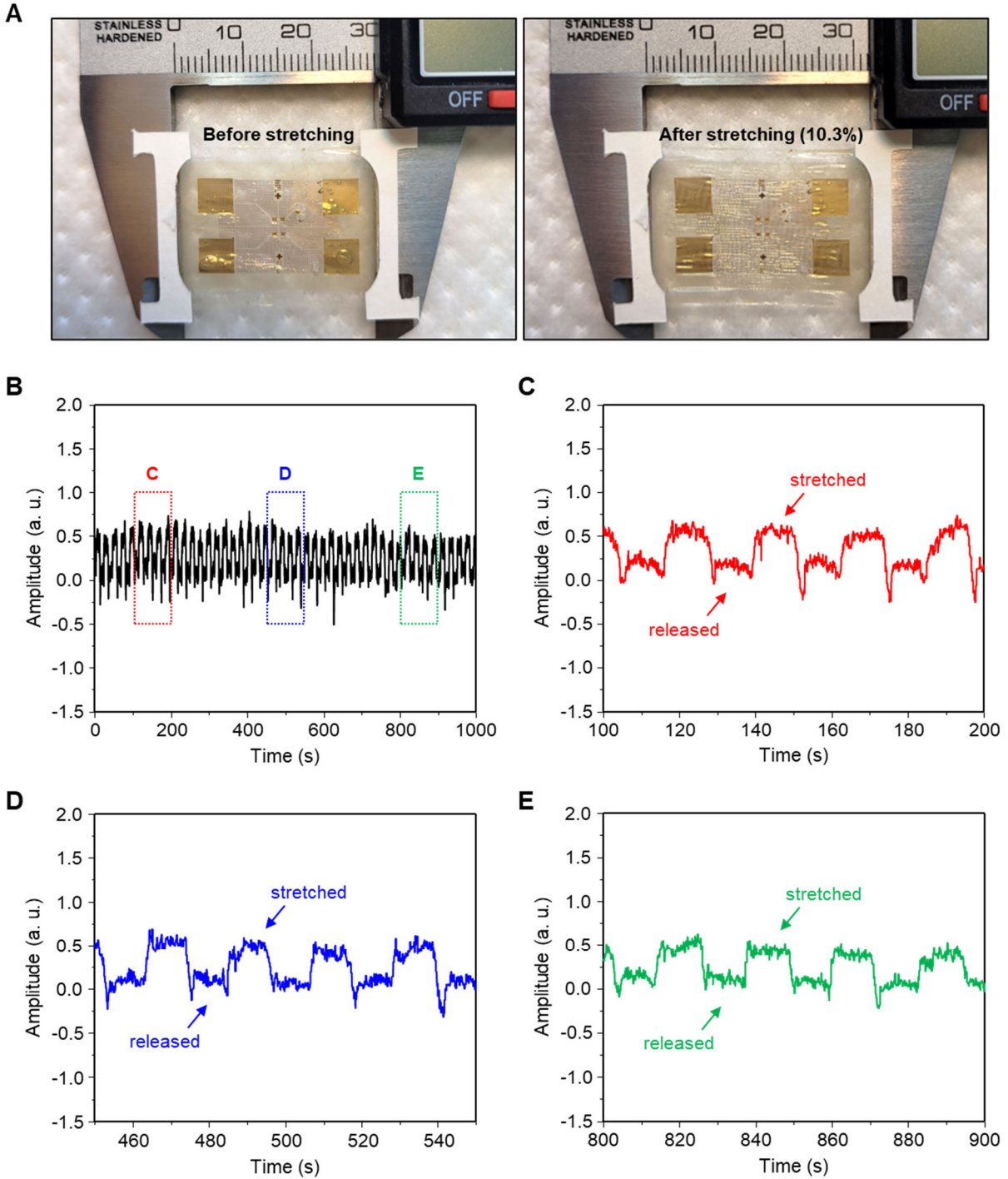
Fig. S16. (A) Photographs of GaN SAW-based e-skin before and after stretching (strain = 10.3 %). **(B)** Wireless recording of GaN SAW-based strain sensor during stretchability test. Continuous wireless recording from GaN SAW-based strain sensor on e-skin throughout 1000 s under the repetitive strain of 10.3 %. **(C-E)** Magnified waveforms of the strain profile at different time points: (C) 100 – 200 s, (D) 450 – 550 s, and (E) 800 – 900 s, respectively.
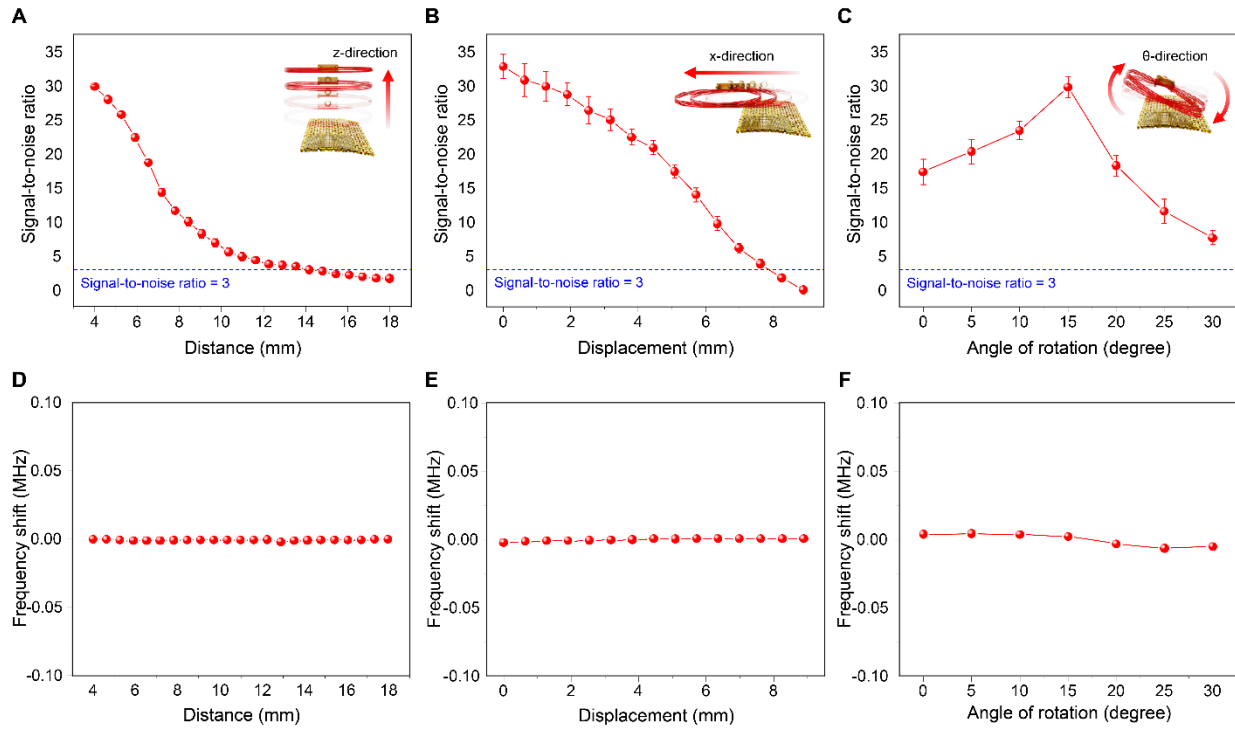
Fig. S17. (A-C) Signal-to-noise ratio measured by GaN SAW-based e-skin device when coil antenna is displaced in (A) z-direction, (B) x-direction, and (C) θ-direction. Displacement in θ-direction was conducted at a 6 mm distance to secure a rotating room for the coil antenna. **(D-E)** Resonant frequency shift when coil antenna is displaced in (D) z-direction, (E) x-direction, and (F) θ-direction.
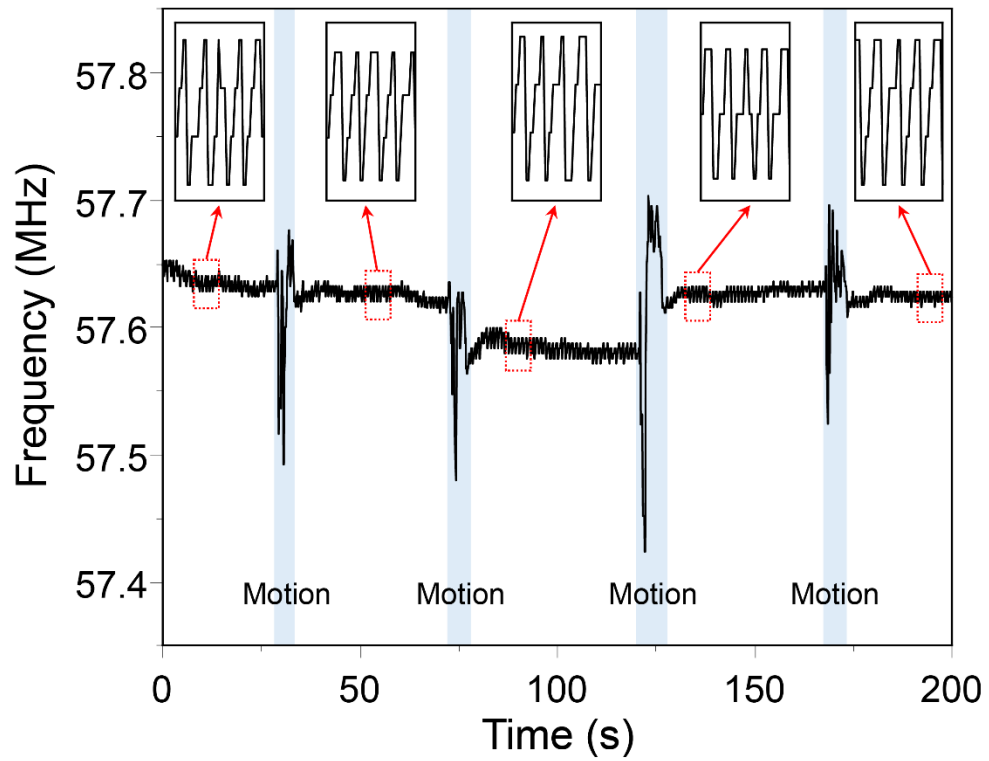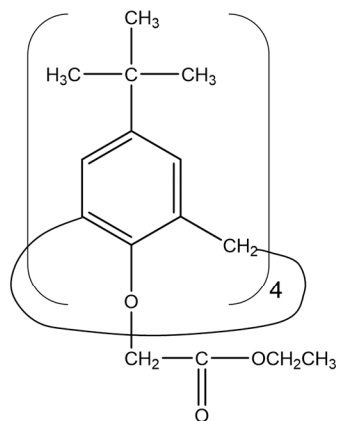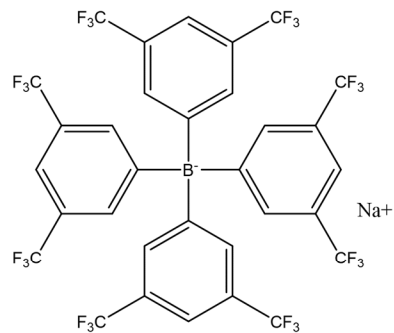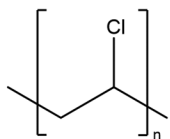
Fig. S18. Heartbeat pulse frequency measurement under body motion. Insets show magnified view of each graph.

4-tert-Butylcalix[4]arene-tetraacetic acid tetraethyl ester (Na ionophore X)

Sodium tetrakis[3,5-bis(trifluoromethyl)phenyl]borate (Na-TFPB, ion-exchanger)

Poly(vinyl chloride) (PVC, base polymer)
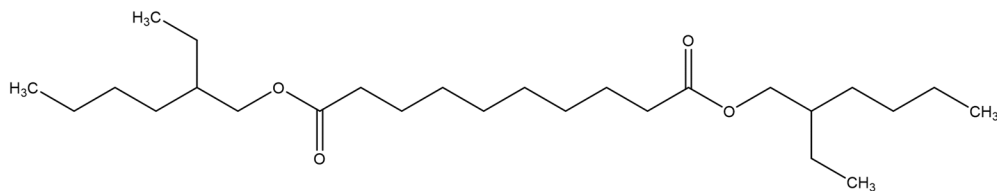
bis(2-ethylhexyl) sebacate (DOS, plasticizer)

Fig. S19. Components of ion-selective membranes (ISMs). These chemicals were dissolved in tetrahydrofuran and spin coated on substrates. The abbreviation and function of each component are written in parentheses.

Fig. S20. Wirelessly recorded SAW ion sensor response towards exposures to aqueous solutions containing different ionic compositions of Na^+, K^+, and Ca^{2+} ions.
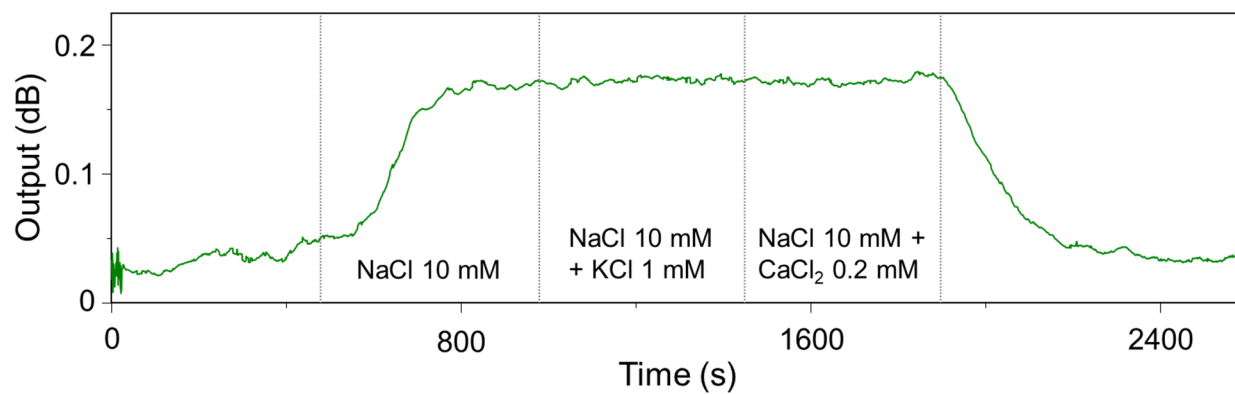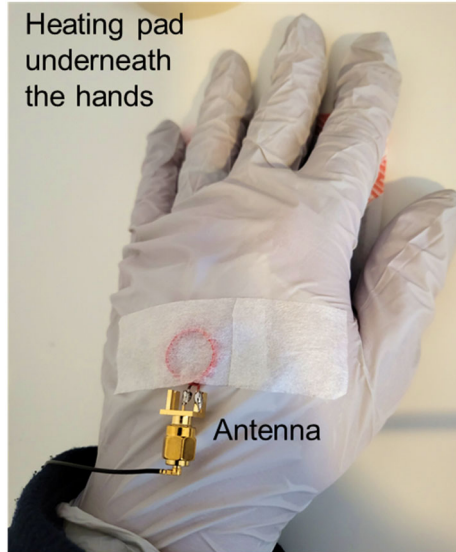
Fig. S21. Photograph of wireless measurement system during *in vivo* sweat measurement. The subject wore a glove on the e-skin-attached hand, and heating pads were placed on the body to generate the sweat.

A

UV light

Polyimide   Polyimide

Electrode 1   Electrode 2

Single-crystalline GaN piezoelectric nanomembrane (200 nm)

Polyimide flexible substrate

Period = 40 μm

B

80 μm

Hole through polyimide.
GaN is exposed.
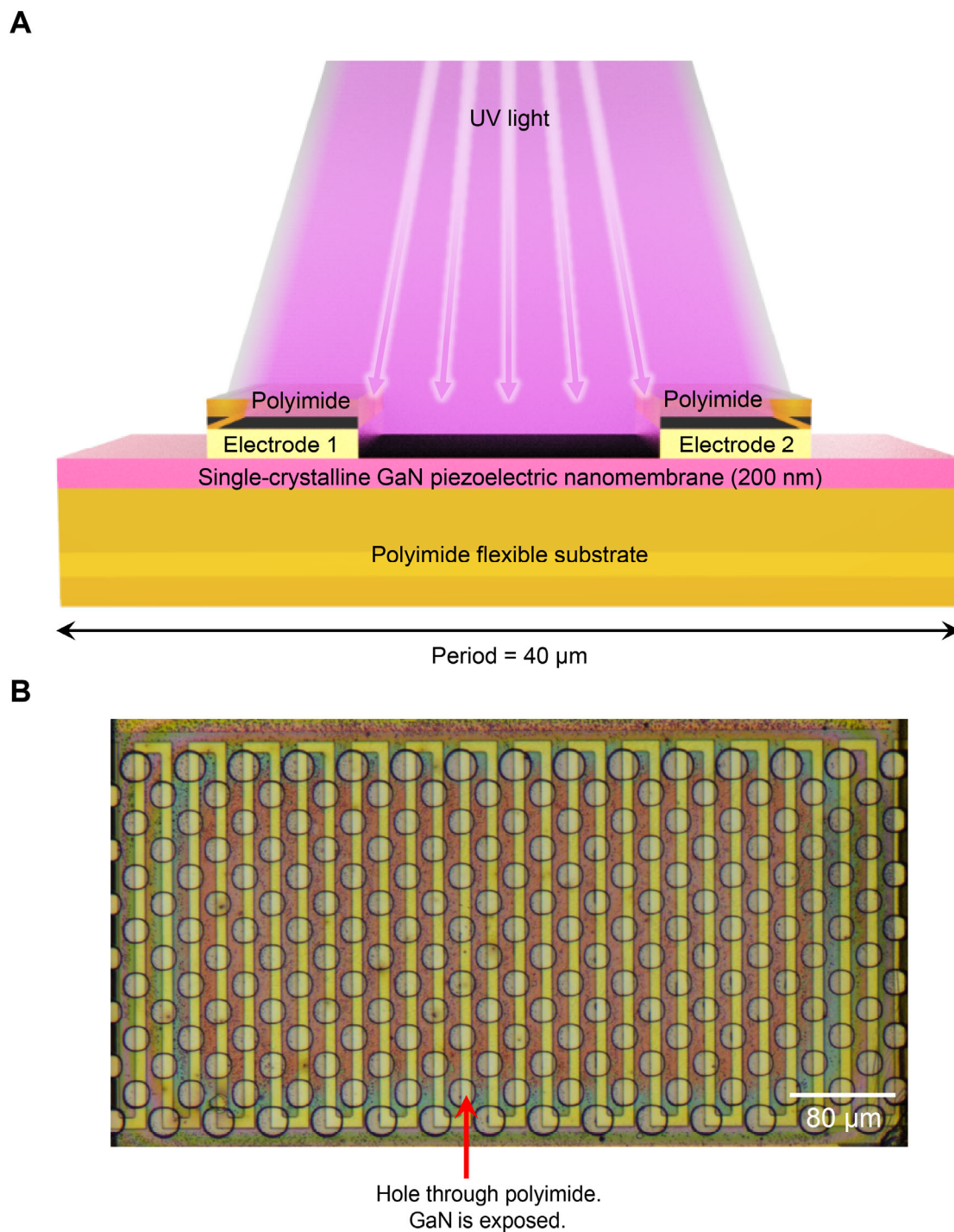
Fig. S22. Wireless GaN SAW UV sensor structure and micrographs. GaN SAW UV sensors received UV light through polyimide through-holes. The absorbed UV light changed the conductivity of the GaN film and modified output responses of GaN SAW UV sensors accordingly. **(A)** The schematics of GaN SAW UV sensors. **(B)** optical micrograph of GaN SAW UV sensors.
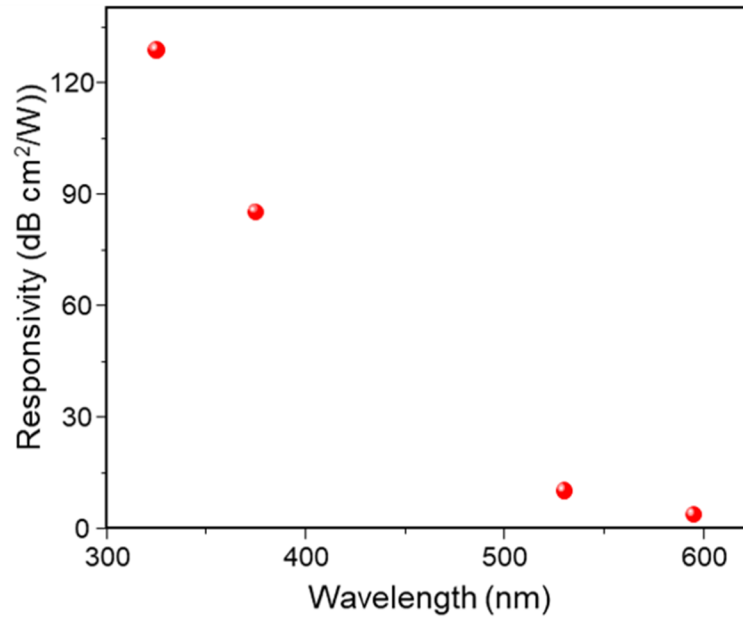
Fig. S23. Responsivities of wireless GaN SAW UV sensors depending on wavelengths of input light. GaN film can absorb mostly UV light, not visible light because of its band gap energy corresponding to a wavelength of 365 nm. Thus, it does not require UV filters for UV sensing application.
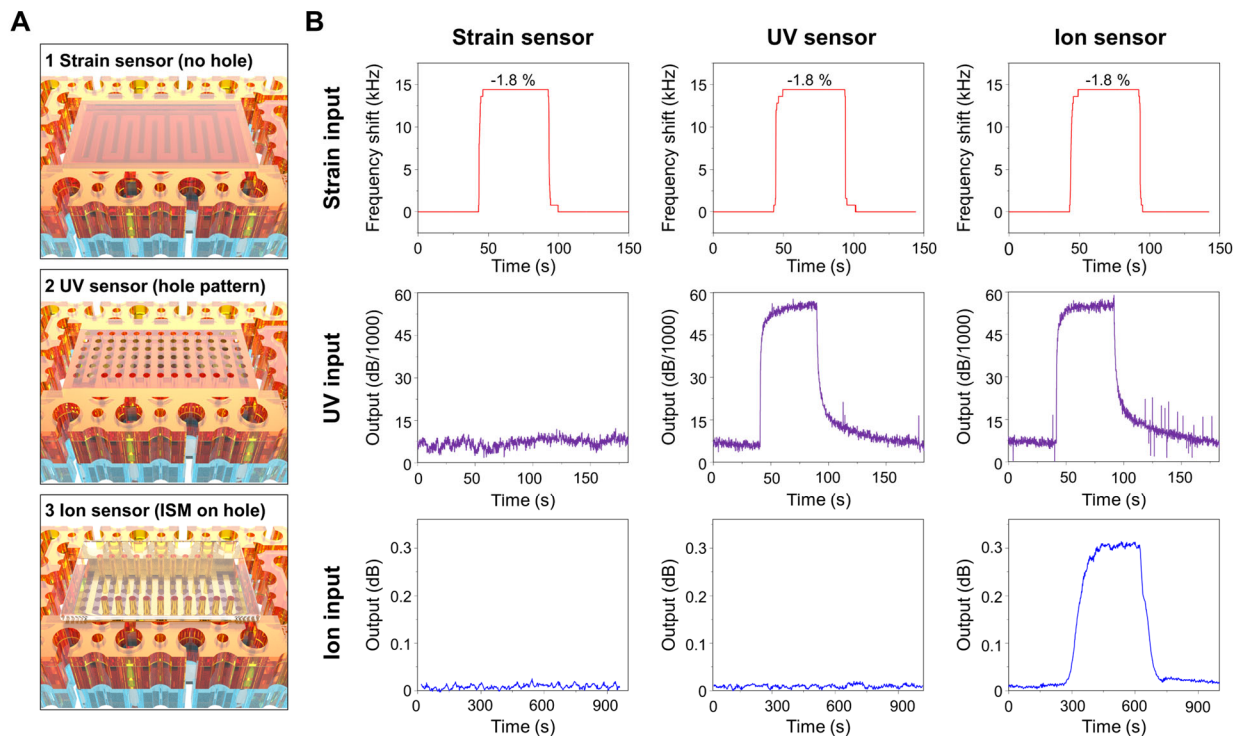
Fig. S24. Evaluation of the responsivities of SAW-based strain, UV light, and ion sensors to variation in each type of stimulus. (A) Schematic illustrations of GaN SAW-based e-skin sensors for strain, UV light, and ion concentration. **(B)** Recorded responses of strain, UV, and ion sensors to variation in each type of input stimuli. The strain, the UV input, and the ion input were -1.8 %, 175 µW/cm^2, and 34 mM NaCl solution, respectively.

	Conventional: chip-based	Soft material-based LC	Our work: Chip-less
System structure	NFC or RFID chip + sensor + antenna	Capacitive sensor + antenna	Surface acoustic wave (SAW) device + antenna
Stretchability	Chip makes non-stretchable region	Whole region is flexible and stretchable	Whole region is flexible and stretchable
Breathability for long-term wearability	Not breathable	Not breathable	Breathable
Conformal contact to skin	Not conformal	Conformal	Conformal
Complexity	>1,000 transistors + sensor device + antenna	Capacitive sensor + antenna	One SAW device + antenna
Energy consumption per measurement	90 nJ to 4 mJ	4 nJ	4 nJ
Wireless communication range	Inductive coupling: coil diameter or a few cm Backscattering: a few m Active RF: tens of m	Inductive coupling: coil diameter or a few cm	Inductive coupling: coil diameter or a few cm Backscattering: a few m

Chemical and bio-sensing		Conventional: chip-based	Soft material-based LC	Our work: Chip-less
Chemical and bio-sensing	Type	Potentiometric	N/A	Mass-based acoustic wave sensing
	Amplification using additives	Not available (small sensible distance due to short Debye length < 7 nm)		Possible (large sensing range > 2 μm)
	Detection of large molecule			

Table S1. Comparison between conventional chip-based wireless e-skin, soft material-based inductor-capacitor (LC) wireless e-skin, and our chip-less surface acoustic wave (SAW)-based wireless e-skin.

Na ionophore X (mg)	1.33	2.71	2.71	2.71	4.30	4.30	4.30
Na-TFPB (mg)	0.67	1.49	1.49	1.49	2.10	2.10	2.10
Na ionophore X / Na-TFPB	2	2	2	2	2	2	2
Na ionophore X + Na-TFPB (mg)	2.0	4.2	4.2	4.2	6.4	6.4	6.4
PVC (mg)	42.54	32.11	41.60	47.90	31.40	40.60	46.80
DOS (mg)	55.46	63.69	54.20	47.90	62.20	53.00	46.80
DOS / PVC	1.3	2.0	1.3	1.0	2.0	1.3	1.0
Na ionophore X + Na-TFPB + PVC + DOS (mg)	100	100	100	100	100	100	100
THF (mL)	1	1	1	1	1	1	1
Film thickness (μm)	2.30	2.30	2.30	2.30	2.30	2.30	2.30
Averaged ion sensor response (Hz)	Not stable	15.66	-47.33	20.33	-33.84	-316.94	-20.00

Na ionophore X (mg)	6.36	6.36	6.36	8.60	8.80	17.20	34.40
Na-TFPB (mg)	3.50	3.50	3.50	4.70	4.50	9.50	18.92
Na ionophore X / Na-TFPB	2	2	2	2	2	2	2
Na ionophore X + Na-TFPB (mg)	9.9	9.9	9.9	13.3	13.3	26.7	53.3
PVC (mg)	30.22	39.10	45.05	29.10	29.00	24.57	15.65
DOS (mg)	59.93	51.00	45.05	57.60	57.60	48.73	31.03
DOS / PVC	2.0	1.3	1.0	2.0	2.0	2.0	2.0
Na ionophore X + Na-TFPB + PVC + DOS (mg)	100	100	100	100	100	100	100
THF (mL)	1	1	1	1	2	1	1
Film thickness (μm)	2.30	2.30	2.30	2.30	0.50	2.30	2.30
Averaged ion sensor response (Hz)	19.77	2.33	-15.67	Not stable	-41.23	27.00	Not stable

Table S2. Compositions of tested ion-selective membranes (ISMs). The information about each component is in Fig. S19. The ISMs were spin coated on top of quartz crystal microbalances (QCM), and their responses to 0.86 M NaCl solution in water were recorded using Biolin Scientific Q-Sense E4 system. We chose the composition of 4.3 mg 4-tert-Butylcalix[4]arene-tetraacetic acid

tetraethyl ester (Na Ionophore X), 2.1 mg sodium tetrakis[3,5-bis(trifluoromethyl)phenyl]borate (Na-TFPB), 40.60 mg polyvinyl chloride (PVC), and 53.00 mg bis(2-ethylehexyl) sebacate (DOS) for GaN SAW e-skin.

References and Notes

1. Y. Lee, J. W. Chung, G. H. Lee, H. Kang, J.-Y. Kim, C. Bae, H. Yoo, S. Jeong, H. Cho, S.-G. Kang, J. Y. Jung, D.-W. Lee, S. Gam, S. G. Hahm, Y. Kuzumoto, S. J. Kim, Z. Bao, Y. Hong, Y. Yun, S. Kim, Standalone real-time health monitoring patch based on a stretchable organic optoelectronic system. *Sci. Adv.* **7**, eabg9180 (2021). doi:10.1126/sciadv.abg9180 Medline

2. D.-H. Kim, J.-H. Ahn, W. M. Choi, H.-S. Kim, T.-H. Kim, J. Song, Y. Y. Huang, Z. Liu, C. Lu, J. A. J. S. Rogers, Stretchable and foldable silicon integrated circuits. *Science* **320**, 507–511 (2008). doi:10.1126/science.1154367 Medline

3. L. Tian, B. Zimmerman, A. Akhtar, K. J. Yu, M. Moore, J. Wu, R. J. Larsen, J. W. Lee, J. Li, Y. Liu, B. Metzger, S. Qu, X. Guo, K. E. Mathewson, J. A. Fan, J. Cornman, M. Fatina, Z. Xie, Y. Ma, J. Zhang, Y. Zhang, F. Dolcos, M. Fabiani, G. Gratton, T. Bretl, L. J. Hargrove, P. V. Braun, Y. Huang, J. A. Rogers, Large-area MRI-compatible epidermal electronic interfaces for prosthetic control and cognitive monitoring. *Nat. Biomed. Eng.* **3**, 194–205 (2019). [doi:10.1038/s41551-019-0347-x](doi:10.1038/s41551-019-0347-x) Medline

4. H. U. Chung, B. H. Kim, J. Y. Lee, J. Lee, Z. Xie, E. M. Ibler, K. Lee, A. Banks, J. Y. Jeong, J. Kim, C. Ogle, D. Grande, Y. Yu, H. Jang, P. Assem, D. Ryu, J. W. Kwak, M. Namkoong, J. B. Park, Y. Lee, D. H. Kim, A. Ryu, J. Jeong, K. You, B. Ji, Z. Liu, Q. Huo, X. Feng, Y. Deng, Y. Xu, K.-I. Jang, J. Kim, Y. Zhang, R. Ghaffari, C. M. Rand, M. Schau, A. Hamvas, D. E. Weese-Mayer, Y. Huang, S. M. Lee, C. H. Lee, N. R. Shanbhag, A. S. Paller, S. Xu, J. A. Rogers, Binodal, wireless epidermal electronic systems with in-sensor analytics for neonatal intensive care. *Science* **363**, eaau0780 (2019). doi:10.1126/science.aau0780 Medline

5. W. Gao, S. Emaminejad, H. Y. Y. Nyein, S. Challa, K. Chen, A. Peck, H. M. Fahad, H. Ota, H. Shiraki, D. Kiriya, D.-H. Lien, G. A. Brooks, R. W. Davis, A. Javey, Fully integrated wearable sensor arrays for multiplexed *in situ* perspiration analysis. *Nature* **529**, 509–514 (2016). doi:10.1038/nature16521 Medline

6. D. Son, J. Lee, S. Qiao, R. Ghaffari, J. Kim, J. E. Lee, C. Song, S. J. Kim, D. J. Lee, S. W. Jun, S. Yang, M. Park, J. Shin, K. Do, M. Lee, K. Kang, C. S. Hwang, N. Lu, T. Hyeon, D.-H. Kim, Multifunctional wearable devices for diagnosis and therapy of movement disorders. *Nat. Nanotechnol.* **9**, 397–404 (2014). doi:10.1038/nnano.2014.38 Medline

7. K. Myny, The development of flexible integrated circuits based on thin-film transistors. *Nat. Electron.* **1**, 30–39 (2018). [doi:10.1038/s41928-017-0008-6](doi:10.1038/s41928-017-0008-6)

8. B. E. Jonsson, "An empirical approach to finding energy efficient ADC architectures," IMEKO TC4 International Workshop on ADC Modelling, Testing and Data Converter Analysis and Design 2011 (IWADC 2011) and IEEE 2011 ADC Forum, Orvieto, Italy, 30 June to 1 July 2011.

9. M. C. Vu, I.-H. Kim, W. K. Choi, C.-S. Lim, M. A. Islam, S.-R. Kim, Highly flexible graphene derivative hybrid film: An outstanding nonflammable thermally conductive yet electrically insulating material for efficient thermal management. *ACS Appl. Mater. Interfaces* **12**, 26413–26423 (2020). doi:10.1021/acsami.0c02427 Medline

10. L. Teng, K. Pan, M. P. Nemitz, R. Song, Z. Hu, A. A. Stokes, Soft radio-frequency identification sensors: Wireless long-range strain sensors using radio-frequency identification. *Soft Robot.* **6**, 82–94 (2019). doi:10.1089/soro.2018.0026 Medline

11. X. Huang, Y. Liu, H. Cheng, W.-J. Shin, J. A. Fan, Z. Liu, C.-J. Lu, G.-W. Kong, K. Chen, D. Patnaik, S.-H. Lee, S. Hage-Ali, Y. Huang, J. A. Rogers, Materials and designs for wireless epidermal sensors of hydration and strain. *Adv. Funct. Mater.* **24**, 3846–3854 (2014). doi:10.1002/adfm.201303886

12. Y. Kim, S. S. Cruz, K. Lee, B. O. Alawode, C. Choi, Y. Song, J. M. Johnson, C. Heidelberger, W. Kong, S. Choi, K. Qiao, I. Almansouri, E. A. Fitzgerald, J. Kong, A. M. Kolpak, J. Hwang, J. Kim, Remote epitaxy through graphene enables two-dimensional material-based layer transfer. *Nature* **544**, 340–343 (2017). doi:10.1038/nature22053 Medline

13. H. Yeon, H. Lee, Y. Kim, D. Lee, Y. Lee, J.-S. Lee, J. Shin, C. Choi, J.-H. Kang, J. M. Suh, H. Kim, H. S. Kum, J. Lee, D. Kim, K. Ko, B. S. Ma, P. Lin, S. Han, S. Kim, S.-H. Bae, T.-S. Kim, M.-C. Park, Y.-C. Joo, E. Kim, J. Han, J. Kim, Long-term reliable physical health monitoring by sweat pore-inspired perforated electronic skins. *Sci. Adv.* **7**, eabg8459 (2021). doi:10.1126/sciadv.abg8459 Medline

14. Q. Hua, J. Sun, H. Liu, R. Bao, R. Yu, J. Zhai, C. Pan, Z. L. Wang, Skin-inspired highly stretchable and conformable matrix networks for multifunctional sensing. *Nat. Commun.* **9**, 244 (2018). [doi:10.1038/s41467-017-02685-9](doi:10.1038/s41467-017-02685-9) Medline

15. L. Shi, S. Nihtianov, Comparative study of silicon-based ultraviolet photodetectors. *IEEE Sens. J.* **12**, 2453–2459 (2012). doi:10.1109/JSEN.2012.2192103

16. R. Velazquez, A. Aldalbahi, M. Rivera, P. Feng, Fabrications and application of single crystalline GaN for high-performance deep UV photodetectors. *AIP Adv.* **6**, 085117 (2016). [doi:10.1063/1.4961878](doi:10.1063/1.4961878)

17. C. R. Gorla, N. W. Emanetoglu, S. Liang, W. E. Mayo, Y. Lu, M. Wraback, H. Shen, Structural, optical, and surface acoustic wave properties of epitaxial ZnO films grown on (01$\bar{1}$2) sapphire by metalorganic chemical vapor deposition. *J. Appl. Phys.* **85**, 2595–2602 (1999). [doi:10.1063/1.369577](doi:10.1063/1.369577)

18. A. Shankar, C.-M. Lin, C. Angadi, S. Bhattacharya, N. Broad, D. G. Senesky, "Impact of gamma irradiation on GaN/sapphire surface acoustic wave resonators," 2014 IEEE International Ultrasonics Symposium, Chicago, IL, USA, 3 to 6 September 2014.

19. S.-H. Lee, H.-H. Jeong, S.-B. Bae, H.-C. Choi, J.-H. Lee, Y.-H. Lee, Epitaxially grown GaN thin-film SAW filter with high velocity and low insertion loss. *IEEE Trans. Electron Dev.* **48**, 524–529 (2001). [doi:10.1109/16.906446](doi:10.1109/16.906446)

20. Z. Chen, D.-C. Lu, X.-H. Wang, X.-L. Liu, P.-D. Han, H.-R. Yuan, D. Wang, Z.-G. Wang, S.-T. He, H.-L. Li, Surface acoustic wave velocity and electromechanical coupling coefficient of GaN grown on (0001) sapphire by metal-organic vapor phase epitaxy. *Chin. Phys. Lett.* **18**, 1418–1419 (2001). [doi:10.1088/0256-307X/18/10/338](doi:10.1088/0256-307X/18/10/338)

21. S. Camou, T. Pastureaud, H. Schenk, S. Ballandras, V. Laude, Guided elastic waves in GaN-on-sapphire. *Electron. Lett.* **37**, 1053–1055 (2001). [doi:10.1049/el:20010668](doi:10.1049/el:20010668)

22. R. Rimeika, D. Ciplys, M. Shur, R. Gaska, M. Khan, J. Yang, Electromechanical coupling coefficient for surface acoustic waves in GaN-on-sapphire. *Phys. Status Solidi B* **234**, 897–900 (2002). doi:10.1002/1521-3951(200212)234:3<897:AID-PSSB897>3.0.CO;2-9

23. G. O'Clock Jr., M. Duffy, Acoustic surface wave properties of epitaxially grown aluminum nitride and gallium nitride on sapphire. *Appl. Phys. Lett.* **23**, 55–56 (1973). [doi:10.1063/1.1654804](doi:10.1063/1.1654804)

24. D. Čiplys, R. Rimeika, R. Gaska, M. S. Shur, A. Khan, J. W. Yang, Effect of metallisation on surface acoustic wave velocity in GaN-on-sapphire structures. *Electron. Lett.* **36**, 591–592 (2000). [doi:10.1049/el:20000415](doi:10.1049/el:20000415)

25. A. D. Mickle, S. M. Won, K. N. Noh, J. Yoon, K. W. Meacham, Y. Xue, L. A. McIlvried, B. A. Copits, V. K. Samineni, K. E. Crawford, D. H. Kim, P. Srivastava, B. H. Kim, S. Min, Y. Shiuan, Y. Yun, M. A. Payne, J. Zhang, H. Jang, Y. Li, H. H. Lai, Y. Huang, S.-I. Park, R. W. Gereau 4th, J. A. Rogers, A wireless closed-loop system for optogenetic peripheral neuromodulation. *Nature* **565**, 361–365 (2019). [doi:10.1038/s41586-018-0823-6](doi:10.1038/s41586-018-0823-6) Medline

26. Y. Gao, Q. Li, R. Wu, J. Sha, Y. Lu, F. Xuan, Laser direct writing of ultrahigh sensitive SiC-based strain sensor arrays on elastomer toward electronic skins. *Adv. Funct. Mater.* **29**, 1806786 (2019). doi:10.1002/adfm.201806786

27. R. Lin, H.-J. Kim, S. Achavananthadith, S. A. Kurt, S. C. C. Tan, H. Yao, B. C. K. Tee, J. K. W. Lee, J. S. Ho, Wireless battery-free body sensor networks using near-field-enabled clothing. *Nat. Commun.* **11**, 444 (2020). [doi:10.1038/s41467-020-14311-2](doi:10.1038/s41467-020-14311-2) Medline

28. O. O. Rakibet, C. V. Rumens, J. C. Batchelor, S. J. Holder, Epidermal passive RFID strain sensor for assisted technologies. *IEEE Antennas Wirel. Propag. Lett.* **13**, 814–817 (2014). doi:10.1109/LAWP.2014.2318996

29. S. Niu, N. Matsuhisa, L. Beker, J. Li, S. Wang, J. Wang, Y. Jiang, X. Yan, Y. Yun, W. Burnett, A. S. Y. Poon, J. B. H. Tok, X. Chen, Z. Bao, A wireless body area sensor network based on stretchable passive tags. *Nat. Electron.* **2**, 361–368 (2019). [doi:10.1038/s41928-019-0286-2](doi:10.1038/s41928-019-0286-2)

30. D.-H. Kim, N. Lu, R. Ma, Y.-S. Kim, R.-H. Kim, S. Wang, J. Wu, S. M. Won, H. Tao, A. Islam, K. J. Yu, T. I. Kim, R. Chowdhury, M. Ying, L. Xu, M. Li, H.-J. Chung, H. Keum, M. McCormick, P. Liu, Y.-W. Zhang, F. G. Omenetto, Y. Huang, T. Coleman, J. A. Rogers, Epidermal electronics. *Science* **333**, 838–843 (2011). doi:10.1126/science.1206157 Medline

31. J. Choi, R. Ghaffari, L. B. Baker, J. A. Rogers, Skin-interfaced systems for sweat collection and analytics. *Sci. Adv.* **4**, eaar3921 (2018). doi:10.1126/sciadv.aar3921 Medline

32. M. K. Kwak, H.-E. Jeong, K. Y. Suh, Rational design and enhanced biocompatibility of a dry adhesive medical skin patch. *Adv. Mater.* **23**, 3949–3953 (2011). doi:10.1002/adma.201101694 Medline

33. J. Kim, Y. Wang, H. Park, M. C. Park, S. E. Moon, S. M. Hong, C. M. Koo, K.-Y. Suh, S. Yang, H. Cho, Nonlinear frameworks for reversible and pluripotent wetting on topographic surfaces. *Adv. Mater.* **29**, 1605078 (2017). doi:10.1002/adma.201605078 Medline

34. M. Villa, R. D. Hale, M. S. Ewing, Effects of fiber volume on modal response of through-thickness angle interlock textile composites. *Open J. Compos. Mater.* **4**, 40–46 (2014). doi:10.4236/ojcm.2014.41005

35. M. Polian, M. Grimsditch, I. Grzegory, Elastic constants of gallium nitride. *J. Appl. Phys.* **79**, 3343–3344 (1996). doi:10.1063/1.361236

36. R. J. Umpleby 2nd, S. C. Baxter, Y. Chen, R. N. Shah, K. D. Shimizu, Characterization of molecularly imprinted polymers with the Langmuir-Freundlich isotherm. *Anal. Chem.* **73**, 4584–4591 (2001). doi:10.1021/ac0105686 Medline

37. J. Kim, P. Gutruf, A. M. Chiarelli, S. Y. Heo, K. Cho, Z. Xie, A. Banks, S. Han, K.-I. Jang, J. W. Lee, K.-T. Lee, X. Feng, Y. Huang, M. Fabiani, G. Gratton, U. Paik, J. A. Rogers, Miniaturized battery-free wireless systems for wearable pulse oximetry. *Adv. Funct. Mater.* **27**, 1604373 (2017). doi:10.1002/adfm.201604373 Medline

38. J. Kim, G. A. Salvatore, H. Araki, A. M. Chiarelli, Z. Xie, A. Banks, X. Sheng, Y. Liu, J. W. Lee, K.-I. Jang, S. Y. Heo, K. Cho, H. Luo, B. Zimmerman, J. Kim, L. Yan, X. Feng, S. Xu, M. Fabiani, G. Gratton, Y. Huang, U. Paik, J. A. Rogers, Battery-free, stretchable optoelectronic systems for wireless optical characterization of the skin. *Sci. Adv.* **2**, e1600418 (2016). doi:10.1126/sciadv.1600418 Medline

39. S. Y. Heo, J. Kim, P. Gutruf, A. Banks, P. Wei, R. Pielak, G. Balooch, Y. Shi, H. Araki, D. Rollo, C. Gaede, M. Patel, J. W. Kwak, A. E. Peña-Alcántara, K.-T. Lee, Y. Yun, J. K. Robinson, S. Xu, J. A. Rogers, Wireless, battery-free, flexible, miniaturized dosimeters monitor exposure to solar radiation and to light for phototherapy. *Sci. Transl. Med.* **10**, eaau1643 (2018). doi:10.1126/scitranslmed.aau1643 Medline

40. S. Han, J. Kim, S. M. Won, Y. Ma, D. Kang, Z. Xie, K.-T. Lee, H. U. Chung, A. Banks, S. Min, S. Y. Heo, C. R. Davies, J. W. Lee, C.-H. Lee, B. H. Kim, K. Li, Y. Zhou, C. Wei, X. Feng, Y. Huang, J. A. Rogers, Battery-free, wireless sensors for full-body pressure and temperature mapping. *Sci. Transl. Med.* **10**, eaan4950 (2018). doi:10.1126/scitranslmed.aan4950 Medline

41. L. Reindl, G. Scholl, T. Ostertag, C. C. W. Ruppel, W.-E. Bulst, F. Seifert, SAW devices as wireless passive sensors. *1996 Proc. IEEE Ultrason. Symp.* **1**, 363–367 (1996). doi:10.1109/ULTSYM.1996.583993

42. P. Gutruf, V. Krishnamurthi, A. Vazquez-Guardado, Z. Xie, A. Banks, C.-J. Su, Y. Xu, C. R. Haney, E. A. Waters, I. Kandela, S. R. Krishnan, T. Ray, J. P. Leshock, Y. Huang, D. Chanda, J. A. Rogers, Fully implantable optoelectronic systems for battery-free, multimodal operation in neuroscience research. *Nat. Electron.* **1**, 652–660 (2018). doi:10.1038/s41928-018-0175-0